1   **Manuscript # 5480 - Revision 2**

2

3   **Degassing of hydrous trachytic Campi Flegrei and phonolitic Vesuvius melts: Experimental**

4   **limitations and chances to study homogeneous bubble nucleation**

5

Oliver Preuss[1], Holger Marxer[1], Sarah Ulmer[1,2], Johannes Wolf[1], and Marcus Nowak*[1]

[1]Department of Geosciences, University of Tuebingen, Wilhelmstraße 56, 72074 Tuebingen,

Germany

[2]Institue for Materials Science, University of Stuttgart, Heisenbergstraße 3, 70568 Stuttgart,

Germany

*corresponding author

postal: Department of Geosciences

               University of Tuebingen

               Wilhelmstraße 56

               72074 Tuebingen

               Germany

e-mail: marcus.nowak@uni-tuebingen.de

phone: +49 7071 29 72648

6   **Abstract**

7   Melt degassing by bubble nucleation and growth is a driving mechanism of magma ascent.

8   Therefore, decompression experiments with hydrous silicate melts were used to investigate the

9   onset and the dynamics of H_2O degassing. Nominally H_2O-undersaturated trachytic Campi

10   Flegrei and phonolitic Vesuvius melts representative for the magma compositions of the Campi

11   Flegrei volcanic system were decompressed at a super-liquidus temperature of 1050 °C from 200

12   MPa to final pressures (P_{final}) of 100, 75 and 60 MPa using continuous decompression rates of

13   0.024 and 0.17 MPa·s^{-1}. Experiments started from either massive glass cylinders or glass powder

14   to demonstrate the influence of the starting material on melt degassing. Glass powder can be used

15   to shorten the equilibration time (t_{eq}) prior to decompression for dissolution of H_2O in the melt.

16   The decompressed samples were quenched and compared in terms of bubble number density

17   (N_V), porosity and residual H_2O content in the melt.

18   Decompression of all glass cylinder samples led to homogeneous bubble nucleation with high

19   N_V of ~10^5 mm^{-3}. The supersaturation pressures for homogeneous bubble nucleation were

20   estimated to be <76 MPa for the trachytic and <70 MPa for the phonolitic melt. In contrast to

21   glass cylinders, the usage of glass powder equilibrated for 24 h before decompression prevented

22   homogeneous bubble nucleation during decompression. We suggest that trapped air in the

23   powder pore space resulted in the formation of tiny H_2O-N_2 bubbles throughout the samples prior

24   to decompression. Degassing of these glass powder samples was facilitated by diffusive growth

25   of these pre-existing bubbles and thus did not require significant H_2O supersaturation of the melt.

26   This is evidenced by several orders of magnitude lower N_V and lower residual H_2O contents at

27   correspondingly higher porosities compared to the glass cylinder samples. However, a significant

28   extension of t_{eq} to 96 h in the glass powder experiments led to degassing results comparable to

2

29   the glass cylinder samples. This effect is probably due to Ostwald ripening, coalescence and the

30   ascent of the pre-existing bubbles during the extended t_{eq} prior to decompression.

31   The N_V of the glass cylinder samples were used to test the applicability of the vesiculation

32   model provided by Toramaru (2006). For the applied decompression rates, the experimental N_V

33   are up to 5 orders of magnitude higher than the values predicted by the model. This may be

34   mainly attributed to the usage of the macroscopic surface tension and the total H_2O diffusivity in

35   the model to describe the molecular process of bubble nucleation. A significant increase in

36   modeled N_V can be achieved by application of a reduced surface tension in combination with the

37   lower diffusivity of network formers as a limiting parameter for the formation of a bubble

38   nucleus.

39   This study demonstrates that the investigation of homogeneous bubble nucleation necessitates

40   an optimized experimental protocol. We strongly recommend to perform experiments with

41   massive glass cylinders as starting material. The timescale of decompression is a limiting

42   parameter and must be short enough to minimize the opportunity for a reduction of N_V by bubble

43   coalescence. Considering our comparably high N_V, the samples of many previous experimental

44   studies that were used to calibrate models for homogeneous bubble nucleation were probably

45   subject to significant N_V reduction. Newly derived data from optimized experiments will require

46   improved models for homogeneous bubble nucleation during magma ascent.

47

48   **Keywords:** Campi Flegrei, magma ascent, decompression experiment, homogeneous bubble

49   nucleation, H_2O degassing, bubble number density

50

51
52

3

53   **Introduction**

54   The Campi Flegrei (CF) are an active volcanic system in the Campanian plain close to the

55   densely populated area of Naples (Italy). The CF volcanism is characterized by mainly explosive

56   activity with both magmatic and hydromagmatic episodes (e.g. Mastrolorenzo and Pappalardo,

57   2006). The main structural feature is a nested caldera that formed during two main collapses

58   (Orsi et al., 1992) related to catastrophic eruptions: the 39 ka Campanian Ignimbrite (CI) and the

59   14 ka Neapolitan Yellow Tuff events. During the CI super-eruption 150-200 km^3 dense rock

60   equivalent of magma were emitted and spread as ignimbrites over 30000 km^2 (De Vivo et al.,

61   2010; Rolandi et al., 2003). A geophysical anomaly beneath the whole Neapolitan area suggests a

62   huge and long-lived deep magma chamber shared by the CF and the Vesuvius stratovolcano,

63   which is in direct neighborhood to the city of Naples (Pappalardo and Mastrolorenzo, 2012). The

64   present bradyseism in the CF indicates magmatic activity that could lead to potentially

65   catastrophic eruptions that threaten millions of people in this highly populated area (De Vivo et

66   al., 2010). Such eruptions are driven by violent magmatic 'degassing'. This term is used to

67   describe the exsolution of a supercritical fluid phase from the ascending magma due to

68   decreasing volatile solubility in the silicate melt. The driving degassing process is the exsolution

69   of H_2O from the melt as main volatile component in most magmatic systems (Sparks, 1978).

70   However, these dynamic degassing processes beneath volcanic systems cannot be observed

71   directly in nature. Therefore, the simulation of magma ascent by decompression experiments with

72   volatile-bearing silicate melts is essential to understand these processes.

73   Pressure (*P*) decrease during magma ascent results in volatile supersaturation in the melt that

74   initiates nucleation and growth of fluid bubbles. These processes cause a substantial density

75   decrease and influence the viscosity of the ascending magma (e.g. Gonnermann and Manga,

76   2007). Therefore, melt degassing is the driving force for increased ascent rates. In volatile-

4

77   saturated magmas, degassing during decompression can be facilitated by growth of pre-existing

78   bubbles. Increasing supersaturation during magma ascent may trigger heterogeneous and/or

79   homogeneous bubble nucleation and growth, depending on the presence of heterogeneous

80   nucleation sites such as crystals. In case of heterogeneous bubble nucleation, the required

81   supersaturation P can be significantly reduced compared to bubble nucleation in a crystal-free

82   homogeneous melt (Hurwitz and Navon, 1994; Toramaru, 1989). Increasing ascent velocities

83   may cause multiple nucleation events due to the change from a diffusion-controlled to a

84   viscosity-controlled regime (Toramaru, 1995). However, the occurrence of multiple nucleation

85   events is also dependent on the bubble number density (N_V) and the size of the pre-existing

86   bubbles (Toramaru, 2014). The bubble nucleation record can also be influenced by Ostwald

87   ripening and coalescence, both reducing N_V (Toramaru, 2006). The complex degassing history of

88   natural volcanic rocks often conceals the record of the onset of degassing. Therefore,

89   homogeneous bubble nucleation has already been investigated in experimental studies (e.g.

90   Gondé et al., 2011; Mangan and Sisson, 2000; Mourtada-Bonnefoi and Laporte, 2002).

91   In many other previous degassing studies glass- or natural volcanic rock powder was used as

92   starting material for decompression experiments (e.g. Gardner et al., 1999; Martel and Iacono-

93   Marziano, 2015; Mastrolorenzo and Pappalardo, 2006; Suzuki et al., 2007). Experiments starting

94   from glass powder and excess H_2O produce numerous small hydration bubbles in the melt prior

95   to decompression. Diffusive growth of such pre-existing hydration bubbles can inhibit nucleation

96   and growth of decompression bubbles in the fluid depleted drainage zone of the hydration

97   bubbles during decompression (Gardner et al., 1999; Larsen and Gardner, 2000). However, pre-

98   existing bubbles in the melt do not exclusively form due to excess H_2O in the capsule. Nominally

99   H_2O-undersaturated starting conditions using glass powder are suggested to produce air (or

100   simplified N_2) bubbles in the melt prior to decompression (Mourtada-Bonnefoi and Laporte,

5

101   2002; Simakin et al., 1999) due to the air in the pore space of the powder, which is entrapped

102   during capsule preparation. These bubbles in the melt may then have the same effect on

103   degassing as pre-existing hydration bubbles and facilitate equilibrium degassing paths during

104   decompression. Thus, it is important to consider the effects of starting material and volatile

105   contents in the experimental samples on degassing.

106   In this study, the H_2O degassing behavior of two magma compositions (a trachyte from the CI

107   super-eruption and a K-phonolite from the Vesuvius AD 79 plinian eruption) was investigated at

108   constant decompression rates to simulate the degassing scenarios of magma compositions

109   representative for the still active Campi Flegrei volcanic system. Decompression experiments

110   starting from glass powder and massive glass cylinders are compared in terms of the onset and

111   extent of degassing. The experimentally derived bubble number densities are used to test the

112   applicability of the vesiculation model of Toramaru (2006), which was developed for

113   homogeneous bubble nucleation at a constant decompression rate. Experimental limitations are

114   outlined and will contribute to improve the investigation of homogeneous bubble nucleation in

115   silicate melts.

116

117   **Experimental and analytical procedures**

118   **Starting material**

119   The starting glasses for all experiments were synthesized by mixing fired oxide (SiO_2, TiO_2,

120   Al_2O_3, FeO, MnO, MgO), dried carbonate ($CaCO_3$, Na_2CO_3, K_2CO_3) and $(NH_4)_2HPO_4$ powders

121   according to the analysis of the CI Triflisco composition (OF17c1-sp) and the Vesuvius "white

122   pumice" composition (VAD79) reported in Civetta et al. (1997) and Iacono Marziano et al.

123   (2007), respectively (Table 1). The powder mixtures were ground and homogenized for 30 min in

124   a zirconia ball mill and fused in a $Pt_{90}Rh_{10}$ crucible for 6 h at 1600 °C. Afterwards, the crucible

6

125   was rapidly quenched in water. The final homogenization was carried out by grinding the glass

126   batches for 20 min in the ball mill and fusing the glass powders for 1 h at 1600 °C. This step

127   leads to the formation of N_2-rich bubbles (due to entrapped air in the pore space of the glass

128   powders) during melting. Most of these bubbles ascended to the surface of the melt batch during

129   fusing. However, it is possible that some N_2-rich bubbles remained in the melts due to the limited

130   fusing timescale. The amount of residual bubbles is also influenced by bubble size and viscosity

131   of the melt that affect bubble ascent. Instead of a rapid quench in water, the melts were cooled

132   down moderately by an air-fan in order to inhibit tension cracks in the glass. The cooling rate was

133   fast enough to prevent the melt from partial crystallization. 6 - 7 mm long cylinders with 5 mm in

134   diameter were drilled out of the glasses and ground at the edges. For the applied decompression

135   rates in this study, Marxer et al. (2015) showed that 5 mm cylinders provide sufficient space for

136   homogeneous bubble nucleation and growth in the capsule center that is unaffected by

137   heterogeneous bubble nucleation processes at the capsule-melt interface and the corresponding

138   diffusional loss of H_2O towards the capsule wall.

139   A calibrated 10 ml pycnometer (±5 μl) was used to determine the porosity of several glass

140   cylinders. The reference densities of the nominally dry, bubble-free glasses were calculated by

141   the model of Appen (1949) modified by Kloess (2000). The resulting density of the CI glass is

142   2508 $g \cdot l^{-1}$ and 2496 $g \cdot l^{-1}$ for the VAD79 glass. The pycnometer density measurements of the CI

143   glass cylinders (2507±15 $g \cdot l^{-1}$, 4 cylinders measured) matched the calculated density for the CI

144   composition and indicate porosities <1 %. The derived porosity of the VAD79 glass cylinders

145   (2403±48 $g \cdot l^{-1}$, 10 cylinders measured) varies between 1 - 6 %. These porosities are confirmed by

146   bubble phase proportions derived from image analysis of halved glass cylinders.

147   After drilling, the residual glasses were crushed and different grain size fractions were

148   separated by sieving. A 1:1 weight fraction mixture of grain sizes from 500 – 200 μm and <200

7

149 μm was used as starting material to minimize the porosity during capsule preparation. The

150 porosity of the powder was determined by complete filling and weighing a cylindrical steel

151 container with 5 mm inner diameter and 10 mm height. The loose powder mixture has a porosity

152 of ~46 %. Compaction of the powder with a piston and a hammer in a cylindrical steel container

153 with 5 mm inner diameter resulted in a porosity of ~29 %, which is suggested to be the initial

154 porosity of powder in the filled capsule.

155

156 **Capsule preparation**

157 Gold-Palladium ($Au_{80}Pd_{20}$) was chosen as capsule material for all experimental runs because

158 of the temperature (T) range of the experiments (1300 – 1050 °C) and to inhibit iron loss from the

159 melt into the capsule material (e.g. Kawamoto and Hirose, 1994). $Au_{80}Pd_{20}$ tubes (inner diameter

160 5 mm, wall thickness 0.2 mm) were cleaned in acetone and annealed at 850 °C under atmospheric

161 conditions over night to soften the material for further processing. All experiments were

162 performed in 13 mm long capsules with a welded lid at the bottom. The capsules were loaded

163 with either glass powder (~220 mg, compacted with a piston) or a glass cylinder (~280 mg) and

164 additional H_2O. The capsule top was crimped with a drill chuck and welded shut. Possible

165 leakage was checked gravimetrically after heating the capsules at 110 °C for at least one hour.

166 Additionally, all capsules were pressurized at room temperature for a few minutes in a cold-seal

167 pressure vessel at 100 MPa with water as pressure medium to ensure the structural integrity of the

168 capsule. A gain of weight due to the infiltration of water into the capsules through microscopic

169 leaks was not observed.

170

171 **Experimental method**

8

172   All experiments were conducted in a vertically operated internally heated argon pressure

173   vessel (IHPV) at intrinsic oxygen fugacity (fO_2) conditions. At H_2O-saturated conditions, the fO_2

174   was determined to be ~3.5 log units above the fO_2 of the quartz-fayalite-magnetite (QFM) solid

175   oxygen buffer (Berndt et al., 2002). The IHPV is equipped with a rapid quench (RQ) device that

176   facilitates a maximum sample cooling rate of approximately 150 $K \cdot s^{-1}$ (Berndt et al., 2002),

177   depending slightly on the mass and the heat conductivity of the capsule. At RQ, the capsule is

178   dropped from the hot spot zone into the cold quench zone of the sample holder. Rapid cooling

179   causes tension cracks in the glassy state. To minimize cracks in the samples, a 55 mm long

180   ceramic filler rod was inserted into the quench zone to slightly reduce the cooling rate during RQ

181   of our experiments. Alternatively, shutting down the furnace while the capsule remains

182   suspended in the hot spot zone quenches a sample with a lower cooling rate of ~150 $K \cdot min^{-1}$ and

183   is referred to as normal quench (NQ) in this study. Both RQ and NQ were performed isobarically.

184

Isobaric experiments

185

186   A set of three isobaric experiments (IB-C-1a, IB-C-b, IB-C-2, Table 2) starting from CI glass

187   cylinders was performed to check the equilibration time (t_{eq}) for a homogeneous dissolution of

188   H_2O within the melt and to characterize the starting conditions just before decompression. The

189   samples with ~4.7 wt% H_2O were run at 200 MPa and 1300 °C for a t_{eq} of 96 h. The equilibration

190   temperature (T_{eq}) of 1300 °C was chosen to keep t_{eq} as short as possible, because the total H_2O

191   diffusion in silicate melts increases exponentially with T (e.g. Nowak and Behrens, 1997). After

192   t_{eq}, one sample was quenched rapidly, whereas the T for the other two samples was lowered to the

193   decompression temperature of 1050 °C. After an additional annealing time of 30 min, these two

194   samples were quenched by either RQ or NQ to investigate the influence of the cooling rate on the

195   hydrous melt. Isobaric experiments with the VAD79 composition (REF02-12) are documented in

196   Marxer et al. (2015).

197   A set of four isobaric experiments with CI glass powder as starting material was conducted at

198   200 MPa and 1300 °C with different H_2O contents (Table 2). These powder samples were

199   equilibrated for 24 h and quenched rapidly. The resulting H_2O-bearing glasses (IB-P-1 to 4) were

200   used to verify the near infrared (NIR) absorption coefficients for the trachytic composition (Table

201   2) given in Fanara et al. (2015). The NIR measurements of the isobaric samples showed that t_{eq}'s

202   of 96 h for cylinders (IB-C-1a, IB-C-b, REF12) and 24 h for powder (IB-P-4) are sufficient to

203   dissolve H_2O in the melt homogeneously.

204

205   **Decompression experiments**

206   Four sets of degassing experiments starting from nominally H_2O-undersaturated conditions

207   using both glass powder and massive cylinders were conducted with identical decompression

208   parameters to investigate the influence of the starting material on melt degassing. CI and VAD79

209   samples were equilibrated with about 4.7 wt% H_2O at 200 MPa and 1300 °C. The t_{eq} was always

210   96 h for experiments starting from glass cylinders. The powder samples were equilibrated for

211   either 24 or 96 h (Table 3) to investigate the effect of t_{eq} on melt degassing. After t_{eq}, the T was

212   lowered to 1050 °C and the samples were annealed for 30 min. Starting from these super-liquidus

213   conditions (Fanara et al., 2012; Iacono Marziano et al., 2007; Marxer et al., 2015), isothermal

214   decompression was performed by continuous P release using a high-pressure low-flow metering

215   valve equipped with a piezoelectric nano-positioning system (Marxer et al., 2015; Nowak et al.,

216   2011). The continuous decompression rate was either 0.024 or 0.17 $MPa \cdot s^{-1}$ down to a final

217   pressure (P_{final}) of 100 MPa. Further glass cylinder samples were decompressed to a lower P_{final}

218   of 75 and 60 MPa (Table 3). At P_{final}, all samples were quenched rapidly at isobaric conditions.

10

219

Sample preparation

221   Several pieces of the CI and VAD79 starting glasses from different locations in the melting

222   crucible were embedded in epoxy resin racks for chemical analysis by electron microprobe

223   (EMP). The surfaces of all racks were ground, polished and coated with carbon using a carbon

224   sputterer. After the experiments, the capsules were checked for weight loss due to possible

225   leakage. The capsules were cut longitudinal along the cylinder axis in two halves. One half was

226   directly embedded in epoxy resin racks for examination with a scanning electron microscope

227   (SEM) to generate high-resolution backscattered electron (BSE) images. The other half of a

228   sample was removed from the capsule, embedded and double-sided ground and polished down to

229   a thickness of 150 - 200 µm for Fourier transform infrared (FTIR) measurements and transmitted

230   light microscopy (TLM).

231

EMP analysis

233   The nominally dry CI and VAD79 starting glasses were analyzed by WDS measurements

234   using a JEOL JXA 8900 R electron microprobe at an accelerating voltage of 15 kV and a beam

235   current of 4 nA. The glasses were analyzed with a defocused beam of 20 µm in diameter to

236   inhibit loss of alkalis (Stelling et al. 2008). The peak counting times were set to 10 s (Na), 16 s

237   (Si, Al, Fe, Mg, Ca, K) and 30 s (Ti, Mn, P). The results of these WDS analyses are presented in

238   Table 1.

239

FTIR spectroscopy

241   The residual total H_2O concentrations of the glasses were determined by NIR measurements

242   with a Bruker Vertex 80v FTIR-spectrometer. A CaF_2 beam splitter and a halogen light source

11

243   were used. The spectrometer is coupled to a Hyperion 3000 IR-microscope with a motorized

244   sample stage, enabling sequences of spatially resolved measurements. NIR absorption spectra

245   from 4000 to 6000 cm^{-1} of the glasses were recorded in transmission mode using a 15x IR

246   Cassegrain objective and an In-Sb single element detector. The spectra were collected with 32 -

247   50 scans at a resolution of 4 cm^{-1}. The spectrometer was evacuated and the microscope was

248   flushed continuously with dried air to minimize influence of atmospheric H_2O. The knife-edge

249   aperture was set to 30x30 (VAD79) or 50x50 μm (CI) and reference spectra were taken without a

250   sample in the beam path. The total H_2O content was determined from the peak heights of

251   absorption bands at 5210 cm^{-1} (molecular H_2O) and 4470 cm^{-1} (OH$^-$) as sum of the species

252   concentrations (e.g. Behrens and Nowak, 2003; Scholze, 1960). Tangential baselines fitting the

253   minima on both sides of each band (Ohlhorst et al., 2001) were used for the trachytic samples. A

254   linear background correction was applied to the phonolitic samples (Iacono Marziano et al.,

255   2007). A Mitutoyo digital micrometer was used to measure the thickness of the samples with an

256   accuracy of 2 - 3 μm. The molar absorption coefficients and the density (ρ) data of the hydrous

257   CI glasses were adopted from Fanara et al. (2015). The absorption coefficients are 0.98(3) and

258   1.19(2) l·mol^{-1}·cm^{-1} for the 5210 and 4470 cm^{-1} band, respectively. The density was calculated by

259   the equation (ρ [g·l^{-1}] = 2457-24·$wt\%$ H_2O) using the gravimetrically determined initial H_2O

260   contents. The corresponding data for the VAD79 composition are provided in Iacono Marziano et

261   al. (2007). The densities of the hydrous VAD79 glasses were calculated by (ρ [g·l^{-1}] = 2470-

262   13·$wt\%$ H_2O) and the molar absorption coefficients are 1.18(11) and 1.14(9) l·mol^{-1}·cm^{-1} for the

263   5210 and the 4470 cm^{-1} bands, respectively. Total H_2O concentration distance profiles of the

264   hydrous glasses of isobaric experiments were monitored by at least 10 individual NIR

265   measurements parallel and perpendicular to the cylinder axis and averaged H_2O contents are

266   presented in Table 2.

267

268 **SEM and 2D image analysis**

269   BSE images of polished sample sections were recorded with a LEO 1450 VP SEM. Each

270 sample was mapped by taking 80 - 130 single images with a resolution of 1024x768 pixels at a

271 magnification of 120 - 300x. Additionally for sample CD-C-5, four different excerpt areas were

272 mapped at a higher magnification of 880 - 1100x. The single images were stitched together and

273 used to determine the bubble number density (N_V) in suitable samples. The bubble number

274 density normalized to pure melt or glass volume (N_V(n)) provides information about nucleation

275 processes during decompression. The bubble intersections were redrawn in a separate image layer

276 and loaded into the ImageJ 1.47 software (Schneider et al., 2012). The bubble intersections were

277 fit with ellipses to determine 2D porosities of the vitrified samples. The axes lengths of the

278 ellipses were imported into the CSDCorrections software (Higgins, 2000) for the calculation of

279 3D porosities and bubble number densities. A detailed description of this method is provided in

280 Marxer et al. (2015).

281   The intersection probability of bubbles (or other objects) in a 2D cut plane decreases with the

282 3D bubble diameter (e.g. Higgins, 2006). The corresponding decrease in the 2D intersection

283 diameter (and in depth of the bubble pit in a polished sample) may complicate proper

284 identification and distinction from other surface features of the specimen. Bubble number

285 densities based on direct 3D sample information may therefore be more reliable in case of very

286 small bubbles on a μm scale. For this study, the N_V-values of samples or parts of samples that

287 contain such small bubbles were determined using transmitted light microscopy.

288

289 **Transmitted light microscopy**

13

290   The NIR samples were also examined with a Zeiss Axio Imager M2m microscope to obtain

291   3D information on N_V in samples with bubbles of only several μm diameter. The microscope is

292   equipped with a motorized sample stage. The Fission Track Studio software "Trackworks"

293   (Autoscan Systems) was used to manually count all observable bubbles in selected sample

294   volumes. The analyzed cuboid volume is confined by the field of view and the thickness of the

295   glass section. The field of view was either 87x65 μm or 175x132 μm depending on the used

296   objective (50x and 100x). The bubble counts were used to calculate the number of bubbles per

297   total unit volume of glass and bubbles per mm^3 (N_V(t)). TLM provides the actual 3D diameters of

298   bubbles (e.g. Gardner et al., 1999). The averaged bubble diameters and the bubble counts were

299   used to estimate the porosities and to calculate the N_V(n) of the samples.

300

301   **Results**

302   **Isobaric experiments**

303   Concentration distance profiles of the hydrous glasses from isobaric experiments measured by

304   FTIR revealed homogeneous distribution of H_2O (averaged H_2O contents presented in Table 2)

305   throughout the glass cylinders without concentration gradients. Examination of the CI and

306   VAD79 starting materials using TLM and SEM revealed that the nominally dry glasses

307   (quenched by air fan cooling) are free of crystals and only contain some air bubbles that resulted

308   from glass synthesis. In contrast, the samples of the isobaric CI experiments with ~4.7 wt% H_2O

309   starting from glass cylinders and powder (IB-C-1a, IB-C-b, IB-P-4, RQ, Table 2) contain

310   numerous, not clearly recognizable objects <1 μm in size. Figure 1a shows small objects in the

311   glass of sample IB-C-1b quenched from 1050 °C. The number density of objects in these RQ

312   samples ranges between $1 \cdot 10^5$ and $4.5 \cdot 10^5$ mm^{-3} (Table 3). The CI sample with ~4.7 wt% H_2O

313   quenched from 1050°C with a cooling rate of about 150 K·min^{-1} (IB-C-2, NQ) shows needle-

14

314   shaped and radially aggregated quench crystals of up to 13 µm length (Figs. 1b and 1c) with an

315   aggregate number density of $7 \cdot 10^4$ mm^{-3}. The rapidly quenched, hydrous VAD79 cylinder sample

316   (REF12, Table 2) is homogeneous without quench crystals or other small objects. The same

317   observation can be made for the two CI samples (RQ) with the lowest H_2O contents of about 1

318   and 2 wt% (IB-P-1 and IB-P-2, Table 2). The samples IB-P-1 to IB-P-4 with different H_2O

319   contents were used to verify the NIR absorption coefficients for the trachytic composition given

320   in Fanara et al. (2015). The measured H_2O contents match the gravimetrically obtained values

321   within error (Table 2).

322

323   **Decompression Experiments**

324   The BSE images of the samples decompressed to a P_{final} of 100 MPa with both

325   decompression rates reveal significant differences in degassing behavior between samples

326   starting from massive glass cylinders and glass powder equilibrated for 24 h prior to

327   decompression (Figs. 2 and 3). Images of the complete halved capsules are provided in the

328   electronic appendix (eFigs. 1-13). The BSE images suggest that cylinder samples are bubble-free,

329   but the TLM images reveal very small bubbles with diameters <4 µm (Figs. 4a and 4c). In

330   contrast, the powder samples, which were equilibrated for 24 h (CD-P-1 and CD-P-24 at 0.17

331   MPa·s^{-1} and CD-P-2a, CD-P-22 at 0.024 MPa·s^{-1}, Fig. 2), show high porosities up to 14 % and

332   are characterized by low $N_V(n)$ of big bubbles (87 - 215 mm^{-3}, Table 3). Moreover, CD-P-1 shows

333   a heterogeneous distribution of these big bubbles and a belt of much smaller bubbles in the center

334   of the sample (Fig. 3, eFigs. 5a and 5b). This results in two different $N_V(n)$-values of 215 mm^{-3}

335   for the big bubbles and $2 \cdot 10^5$ mm^{-3} for the belt of small bubbles. The corresponding glass

336   cylinder samples (CD-C-1, CD-C-23 at 0.17 MPa·s^{-1} and CD-C-2, CD-C-25 at 0.024 MPa·s^{-1},

337   Fig. 2) reveal very high $N_V(n)$ of $2 \cdot 10^5$ to $6 \cdot 10^5$ mm^{-3} with bubble diameters of 1 - 4 µm that result

15

338   in porosities <1 %. These small bubbles are not observable in BSE images (Figs. 2 and 3).

339   Transmitted light images of CD-C-1 and CD-C-2 exhibit small objects in the vicinity of bubbles

340   to which the bubble surface is extended by a thin neck (Fig. 5). In contrast to the powder

341   experiments with a t_{eq} of 24 h, the samples CD-P-2b and CD-P-32 that were equilibrated for 96 h

342   (Figs. 2 and 4) show the same degassing texture of small bubbles with high N_V(n) of $2 \cdot 10^5$ to

343    $3 \cdot 10^5$ mm^{-3} as the corresponding glass cylinder samples (CD-C-2 and CD-C-25) (Figs. 2 and 4).

344   The CI glass cylinder samples decompressed to a P_{final} of 75 MPa (CD-C-3 at 0.024 MPa·s^{-1}

345   and CD-C-4 at 0.17 MPa·s^{-1}, Fig. 6) are characterized by higher porosities and bigger bubble

346   sizes. Within error, the N_V(n)-values are similar to those of the cylinder samples quenched at a

347   P_{final} of 100 MPa (Table 3). The BSE image of sample CD-C-4 suggests that bubbles are limited

348   to the lower part of the glass cylinder (Fig. 6 and eFig. 3a). However, both specimens (CD-C-3,

349   CD-C-4) also contain homogeneously distributed small bubbles (<4 μm) in the upper part of the

350   cylinder similar to CD-C-2 (Fig. 4a). The bubbles located at the capsule-melt interface in CD-C-3

351   (Fig. 6, eFigs. 2a and 2b) are more numerous and clearly bigger than the corresponding bubbles

352   in CD-C-4 (Fig. 6, eFigs. 3a and 3b), which was decompressed with the higher decompression

353   rate. The capsule lid at the bottom of CD-C-3 is not decorated with bubbles. Instead, this sample

354   features some big bubbles in the center of the glass cylinder. The sample area around each of

355   these big bubbles is free of the small bubbles (excerpt Fig. 6).

356   The CI glass cylinder sample CD-C-5 decompressed to a P_{final} of 60 MPa at 0.17 MPa·s^{-1} was

357   removed from the capsule during sample preparation. The bubbles located at the former capsule-

358   melt interface are therefore only partly visible (Figs. 7a and 7b, eFigs. 1a and 1b). The BSE

359   image suggests a homogeneous distribution of bubbles with an average diameter of 8 μm within

360   the sample, but the TLM image of the whole sample (Fig. 7b) reveals convection patterns, which

361   are suggested to be induced by a density gradient due to massive bubble nucleation. The porosity

16

362 and the N_V(n)-values were obtained from the BSE images using the CSDCorrections software

363 (Higgins, 2000). The mean N_V(n)-value of $\sim 7 \cdot 10^5$ mm^{-3} (average of four different areas

364 containing more than 400 bubble intersections) is comparable to the N_V(n)-of the cylinder

365 samples decompressed to a P_{final} of 75 and 100 MPa (Table 3). The mean porosity of ~10 % is the

366 highest of all decompressed cylinder samples. The bubble size distribution (BSD) of sample area

367 4 is characterized by a near-linear trend with a narrow size range from 3 to 13 μm (Fig. 7c).

368   The equilibrium solubility of H_2O at a P_{final} of 100 MPa and 1050 °C is ~3.5 wt% for both the

369 CI and the VAD79 composition (Fanara et al., 2015; Iacono Marziano et al., 2007). The

370 measured H_2O contents of samples originating from glass powder with a t_{eq} of 24 h and a P_{final} of

371 100 MPa are closer to the equilibrium H_2O content than the cylinder samples (Table 3). NIR

372 measurements of the highly vesiculated glass cylinder and powder samples with a t_{eq} of 96 h

373 result in values close to the initial H_2O concentration prior to decompression. This also applies

374 for the CI cylinder samples decompressed to a P_{final} of 75 MPa (Table 3). In the upper part of the

375 sample CD-C-3 (Fig. 6, eFigs. 2a and 2b), where the homogeneously distributed small bubbles

376 are present in the volume measured by NIR, the measured H_2O content (~4.57 wt%) is near the

377 initial H_2O content of 4.78 wt%. One exception is the bubble-depleted area around the big

378 bubbles in this sample (excerpt Fig. 6). The residual H_2O content of the pure glass in the bubble-

379 depleted zone (~3 wt%, Table 3) is close to the extrapolated solubility of the CI melt at 75 MPa

380 (2.89 wt%) as derived from the solubility data of Fanara et al. (2015). The residual H_2O content

381 of sample CD-C-5 decompressed to a P_{final} of 60 MPa could not be determined by NIR

382 measurements due to high N_V(n)-values of $\sim 7 \cdot 10^5$ mm^{-3}. The calculated residual H_2O content of

383 ~3.2 wt% derived from the corrected melt porosity is still higher than the extrapolated

384 equilibrium solubility at 60 MPa (2.61 wt%).

385

Discussion

Quench crystal formation

386
387

388   The NQ isobaric experiment resulted in the formation of quench crystal aggregates consisting

389   of ~13 μm long needle-shaped crystals in the CI melt containing ~4.7 wt% H_2O (Fig. 1b). We

390   suggest that the smaller, unidentified objects in the corresponding RQ isobaric experiments with

391   the CI melt (~4.7 wt% H_2O, both powder and cylinder, both quenched from 1050 and 1300 °C)

392   are also crystals that formed during cooling (Fig. 1a). The RQ samples from the two isobaric CI

393   experiments with the lowest H_2O contents in the melt do not contain any objects. Thus, the

394   effectiveness of quench crystal formation is controlled by the cooling rate and the H_2O content of

395   the melt that influences the glass transition temperature (T_g) (Dingwell and Webb, 1990; Morizet

396   et al., 2007). A faster cooling rate leads to a higher T_g, whereas a higher H_2O content in the melt

397   reduces T_g. The quench crystals in the RQ samples of isobaric experiments with 4.7 wt% H_2O are

398   smaller than those in the NQ sample, because the time for crystallization is shorter. Furthermore,

399   diffusivity of components required for crystal formation and growth decreases with decreasing

400   H_2O content of the melt (Koepke and Behrens, 2001). This explains the absence of any detectable

401   quench crystals in the nominally dry starting material and the two isobaric CI experiments with

402   the lowest H_2O contents in the melt. The VAD79 samples do not contain any detectable quench

403   crystals (Table 1). The small differences in CI and VAD79 bulk composition have a negligible

404   influence on T_g but obviously have an impact on crystal nucleation and crystallization kinetics.

405   Both the starting glass and other samples of isobaric experiments (REF02-06 and REF12 from

406   Marxer et al., 2015) do not contain any detectable crystals.

407   The number densities of quench crystals aggregates (N_C) in the samples of the isobaric CI

408   experiments are within the same order of magnitude (~10^5 mm^{-3}) as the N_V of the bubbles in the

409   cylinder samples decompressed to 100 MPa (Tables 2 and 3). On a first glance, this could be a

18

410   hint that the bubbles in the decompressed CI cylinders nucleated heterogeneously on the quench

411   crystals and initiated degassing during cooling. However, crystals can also nucleate

412   heterogeneously on the surface of bubbles (Davis and Ihinger, 1998). Some of the decompressed

413   CI samples contain bubbles that are connected to smaller objects by a thin neck (Fig. 5). These

414   objects are suggested to be quench crystals, probably magnetite which is liquidus-phase at $T \leq$

415   1000 °C in the CI system (Fanara et al., 2012). Similar bubbles connected by a neck to oxide

416   microlites that were already present in the melt during decompression were observed by Hurwitz

417   and Navon (1994). They presumed that this unstable bubble neck forms due to the shrinkage of

418   the H_2O-filled bubble during isobaric RQ, which has been investigated further by Marxer et al.

419   (2015). A significant volume reduction of a bubble is only expected, if the bubble already existed

420   prior to RQ. Considering the size of the bubble in comparison to the crystal, it would be

421   conceivable that the crystals found in the decompressed CI samples formed at a later stage on the

422   surfaces of existing bubbles and did not affect melt degassing. Quench crystals were not observed

423   in sample CD-C-5 decompressed to a P_{final} of 60 MPa. The absence of quench crystals in this

424   sample is further proof that crystals observed in some samples of isobaric experiments (Table 2)

425   and decompression experiments (Table 3) formed after the nucleation of bubbles during quench.

426   However, small quench crystals <1 μm might not be visible by TLM due to high $N_V(n)$ in

427   combination with bigger mean bubble diameters. The $N_V(n)$-values of the decompressed CI

428   cylinders are also comparable to those determined in the corresponding VAD79 samples (Table

429   3), which do not show any evidence of quench crystal formation. Even if heterogeneous bubble

430   nucleation during quench occurred, it does not affect the principle observations and

431   interpretations made for the comparison of the different starting materials glass powder and

432   massive glass cylinders.

433

The powder problem

Previous studies already indicated that glass powder as starting material might not be appropriate to study bubble nucleation processes in silicate melts (e.g. Gardner et al., 1999; Iacono Marziano et al., 2007; Mourtada-Bonnefoi and Laporte, 2002; Simakin et al., 1999). The degassing process can be influenced by the growth of pre-existing bubbles in the capsule prior to decompression. Hydration bubbles (Gardner et al., 1999) in our samples were avoided by starting from nominally H_2O-undersaturated conditions, but the reduction of additional water in the capsule increases the pore volume in powder samples that is filled with air.

The amount of entrapped air (assumed as 100 % N_2) in the capsules of our experiments can be calculated considering the capsule dimensions, the pure glass volume and the amount of added water. Once sealed, the capsules have a total free volume of about 157 mm^3. The compacted glass powder has a porosity of ~29 %. Assuming that the whole free capsule volume is filled with ~220 mg powder and considering ~11 mm^3 of added water for samples with 4.7 wt% H_2O, the pore volume is at least ~35 mm^3. This corresponds to ~177 ppm N_2 at atmospheric conditions. The calculated amounts of entrapped N_2 are minimum values for optimal powder compaction assuming no free volume in the capsule headspace above the sample. During heating and melting, the H_2O-N_2 fluid mixture (X_{H2O} near 1) in the pore space will form bubbles throughout the whole sample. After preferential dissolution of H_2O, H_2O-N_2 bubbles with slightly decreased X_{H2O} (fluid) will remain in the melt. The usage of a more fine-grained powder leads to smaller pores and probably smaller H_2O-N_2 bubbles in the melt after equilibration, but the total porosity will not decrease. If pre-hydrated glass powder is used as starting material this problem is even more severe (e.g. Fiege et al., 2014), because the amount of enclosed N_2 is higher due to lacking water in the powder pore space prior to the decompression experiments.

20

457   If massive glass cylinders are used, the free volume in the capsule is lower. Cylinders used in

458   this study were 5 mm in diameter and 6.5 mm in height resulting in a volume of ~127 mm^3. To

459   attain H_2O contents of about 4.7 wt% in the melt, ~13 mm^3 H_2O have to be added considering a

460   cylinder weight of ~280 mg. The remaining free volume of at least 17 mm^3 in our capsules

461   contained ~86 ppm N_2. But in contrast to glass powder, the N_2 is enclosed in the headspace of the

462   capsule or free volumes at the sample-capsule interface that will form one or more bigger

463   bubbles, if the glass cylinder is free of air bubbles. The amount of N_2 in experiments starting

464   from cylinders increases, if the glass contains a residual porosity due to the synthesis from

465   powder at 1600 °C. The amount of entrapped N_2 in porous glass cylinders was estimated from

466   density measurements with the pycnometer. A maximum porosity of 6 % for the VAD79 glass

467   cylinders would result in only ~3 ppm trapped N_2 under atmospheric conditions. This calculation

468   is based on the assumptions, that the bubbles in the synthesized batch contain 100% N_2 and that

469   the bubble sizes are preserved at T_g of 665 °C during a moderate quench at atmospheric

470   conditions. T_g was calculated for a residue of 0.1 wt% H_2O in the melt using the model of

471   Giordano et al. (2008). Further cooling of the porous glass to ambient T reduces P_{N2} in the

472   bubbles of the glass batch to ~30 kPa and the trapped amount of N_2 is correspondingly low. N_2-

473   filled bubbles in the glass cylinders are therefore far less critical than the powder pore space.

474   However, higher porosities in glass cylinders could still lead to problems, if the entrapped

475   amount N_2 within the cylinder sample does not completely dissolve in the melt prior to

476   decompression.

477   To date only few studies about nitrogen solubility in hydrous silicate melts were performed

478   for the applied P-T and fO_2 range (Carroll and Webster, 1994; Libourel et al., 2003; Miyazaki et

479   al., 2004; Roskosz et al., 2013). N_2 and Ar have comparable atomic/molecular dimensions and

480   comparable solubility (Carroll and Webster, 1994). The similarity in solubility supports the view

21

481 that nitrogen dissolves physically in silicate melts at QFM+3.5 as non-reactive N_2 molecules

482 (Libourel et al., 2003). The N_2 solubility is reported to be a few ppm at 0.1 MPa (Libourel et al.,

483 2003; Roskosz et al., 2013) and increases up to 150 ppm per 100 MPa (Carroll and Webster,

484 1994). Due to lacking N_2-H_2O solubility data, a solubility model of H_2O-N_2 fluid mixtures (Fig.

485 8) was assumed on the basis of the experimentally determined H_2O-CO_2 solubility reported in

486 Fanara et al. (2015) for the CI composition. These data illustrate that the CO_2 solubility in the CI

487 melt is very low near H_2O-saturated conditions at 200 MPa. Applied to our nominally slightly

488 H_2O-undersaturated starting conditions prior to decompression, it is likely that only about 100

489 ppm of the entrapped N_2 will dissolve in the melt at 200 MPa and 1050 °C (Fig. 8). The few ppm

490 N_2 that are trapped in the bubbles of the glass cylinders should therefore easily dissolve together

491 with H_2O and not interfere significantly with melt degassing during decompression. In case of

492 glass powder as starting material, the calculated amount of entrapped N_2 (~177 ppm) will lead to

493 H_2O-N_2 bubbles with a high X_{H2O} (fluid) of ~0.9 that are distributed throughout the whole

494 sample. However, bubbles in the TLM images of the isobaric experiments using powder as

495 starting material could not be observed due to possibly small diameters <1 µm. Pre-existing

496 bubbles in the melt of powder samples will grow by volatile diffusion into the bubbles as soon as

497 the melt becomes supersaturated during decompression. At sufficiently high number densities of

498 pre-existing bubbles, this degassing process can inhibit homogeneous nucleation of bubbles in the

499 melt in case of a diffusion-controlled growth regime (Mourtada-Bonnefoi and Laporte, 2002;

500 Toramaru, 1995). It is therefore possible that one of the major controlling factors of previous

501 degassing experiments was the usage of glass powder (e.g. Fiege et al., 2014; Mastrolorenzo and

502 Pappalardo, 2006; Suzuki et al., 2007).

503

504 **Decompression experiments (P_{final} = 100 MPa)**

22

505   Although all experiments were performed at nominally H_2O-undersaturated conditions, the

506   comparison between decompressed cylinder samples of both compositions and their powder

507   equivalents equilibrated for 24 h documents that melt degassing is massively influenced by the

508   starting material due to the probable presence of pre-existing bubbles in the powder samples. In

509   case of the cylinder samples, the melt is bubble-free prior to decompression. Thus, the onset of

510   melt degassing is delayed until the energetic barrier for the formation of the new phase boundary

511   is exceeded by reaching the critical supersaturation P to trigger homogeneous bubble nucleation

512   (ΔP_{HoN}). This energetic barrier can be expressed as the free energy of formation (ΔF_c) of a bubble

513   nucleus with critical radius:

$$\Delta F_c = \frac{16\pi\sigma^3}{3\Delta P_{ss}^2} \tag{1}$$

514   and is strongly dependent on the surface tension (σ) of the melt as well as ΔP_{ss} (difference

515   between vapor P in the melt and exterior P) (Hirth et al., 1970). In case of heterogeneous

516   nucleation on crystals or the capsule-melt interface, this energy is lowered with the result that

517   degassing is initiated at a lower ΔP_{ss} in the melt (Hurwitz and Navon, 1994). After nucleation, the

518   bubbles can grow by volatile diffusion and expansion. Both of these growth processes only

519   increase the bubble volumes and do not affect the $N_V(n)$ of the sample.

520   The equilibrium porosity (using Eqn. 5 in Gardner et al., 1999) is ~14 % in the melts (CI and

521   VAD79 composition) for an initial H_2O content of ~4.7 wt% at a P_{final} of 100 MPa and 1050 °C.

522   The equilibrium solubility of H_2O at 100 MPa in both melts is ~3.5 wt% (Fanara et al., 2015;

523   Iacono Marziano et al., 2007). At this P_{final}, the cylinder samples only contain very small bubbles

524   (Fig. 4) with high $N_V(n)$-values of $1\cdot10^5$ to $5\cdot10^5$ mm^{-3} (Table 3). Within error, the measured H_2O

525   contents in the cylinder samples correspond to the initial contents, because numerous small

526   bubbles in the samples have inhibited the NIR measurements of the residual H_2O dissolved in the

23

527   glass. However, the low corrected porosities of <2 % in the melts (Table 3) corresponding to

528   <0.15 wt% degassed H_2O are also proof for high residual total H_2O contents. This documents a

529   high supersaturation in the melt prior to quench and confirms delayed, late-stage bubble

530   nucleation. Porosities close to equilibrium conditions are only reached in the decompression

531   experiments using glass powder that were equilibrated for 24 h (Table 3). The NIR measurements

532   of dissolved H_2O in these glasses also confirm that the melt degassed more efficiently than in

533   experiments with cylinders. Degassing of the powder experiments equilibrated for 24 h was

534   facilitated by growth of tiny pre-existing H_2O-N_2 bubbles and started with the onset of

535   decompression. These bubbles grew during decompression to 100 MPa by volatile expansion and

536   H_2O diffusion into bubbles resulting in low bubble number densities in these experiments (Table

537   3). In comparison to the cylinder specimens, the low residual H_2O contents of the powder

538   samples suggest a near-equilibrium degassing path for both applied decompression rates. Only

539   sample CD-P-1 (Table 3) shows higher H_2O contents in the narrow belt in the middle of the

540   capsule that is occupied by numerous small bubbles (Fig. 3) which may indicate homogeneous

541   bubble nucleation. This feature may be an artifact from powder compaction and H_2O loading

542   leading to the different degassing textures within the sample. In any case, the contrasting bubble

543   textures in CD-P-1 do not support the usability of glass powder equilibrated for only 24 h.

544   Decompression experiments starting from glass powder with a t_{eq} of 96 h show a degassing

545   behavior of the melt that is comparable to the corresponding glass cylinder samples (Fig. 4). We

546   suggest that this observation is due to growth and ascent of the H_2O-N_2 bubbles during

547   equilibration, resulting in a bubble-free melt prior to decompression. Bubble ascent in the melt is

548   generally facilitated by buoyancy due to differences in density of the volatile phase and the

549   surrounding melt. Additionally, the viscosity of the melt and the bubble size are the controlling

550   factors of this process. The ascent of a bubble in a melt can be described by Stokes' Law:

24

$$v_{bubble} = \frac{2r^2 (\rho_{melt} - \rho_{fluid}) \cdot g}{9\eta}$$

(2)

551   where v_{bubble} is the ascent velocity, r is the bubble radius, ρ_{melt} and ρ_{fluid} are the densities of the

552   melt and the fluid (assumed to be 100 % H_2O), g is 9.81 m·s^2 and η is the viscosity of the melt

553   (Berlo et al., 2011). Equation 2 was used to calculate the ascent distance of bubbles as a function

554   of bubble diameter for two temperatures (1050 and 1300 °C) and two t_{eq}´s (24 and 96 h) (Fig. 9).

555   For simplification, we assume instant volatile saturation of the melt at the beginning of the

556   equilibration period in the powder experiments due to small grain sizes. The viscosity of the

557   hydrous CI melt with 4.7 wt% H_2O was calculated after Misiti et al. (2011) to be 77 Pa·s at 1050

558   °C and 4 Pa·s at 1300 °C. The viscosities of the hydrous VAD79 melt at these temperatures are

559   slightly lower, respectively. The corresponding densities of H_2O were calculated using the model

560   of Duan and Zhang (2006) to be 311 g·l^{-1} (1050 °C) and 254 g·l^{-1} (1300 °C) at 200 MPa. For a

561   calculated melt density of 2255 g·l^{-1} (Ochs and Lange, 1999), a bubble with 1 µm in diameter

562   would rise only ~2 µm in the hydrous CI melt at 1050 °C in 96 h. At 1300 °C the same bubble

563   would ascent 43 µm in the same time. A pre-existing bubble in our powder experiments has to

564   rise ~6.5 mm from the bottom to the top of the capsule during a t_{eq} of either 24 or 96 h at 1300 °C

565   (Fig. 9). A timescale of 96 h in our low-viscosity melts most likely facilitates growth of the H_2O-

566   N_2 bubbles that results in increased ascent velocities. In situ investigation of vesiculated basaltic

567   melt by Masotta et al. (2014) demonstrates a timescale for Ostwald ripening of about 50 s.

568   Ostwald ripening requires different internal bubble pressures that correspond to different bubble

569   sizes. These P differences increase exponentially with decreasing bubble sizes (Young-Laplace

570   relation). In addition to coalescence, Ostwald ripening may therefore be a conceivable process for

571   growth of the pre-existing tiny bubbles. A diameter of 12 µm is required for a bubble to ascend

572   from the bottom lid to the capsule top. We suggest that a t_{eq} of 24 h in our powder experiments is

25

573   not sufficient to cause significant bubble growth by ripening and coalescence to accelerate the

574   ascent of the pre-existing bubbles during equilibration. Small H_2O-N_2 bubbles therefore remain in

575   the melt and cause immediate degassing by growth of these bubbles at the onset of

576   decompression. In case of the powder experiments with a t_{eq} of 96 h, the melt is bubble-free prior

577   to decompression and melt degassing is delayed until supersaturation facilitates the nucleation of

578   new H_2O-rich bubbles. This is supported by the NIR measurements and the porosities of the

579   decompression experiments using glass powder equilibrated for 96 h that document a high

580   residual H_2O content in the melt on the level of the cylinder samples (Table 3).

581

582   **Decompression experiments (P_{final} = 75 – 60 MPa)**

583   The glass cylinder samples decompressed to a P_{final} of 75 MPa are characterized by higher

584   porosities and slightly lower N_V(n)-values than the cylinder samples quenched at a P_{final} of 100

585   MPa. In consideration of the small differences in bubble size, coalescence is suggested to be the

586   dominant process that reduces bubble number density in our samples during decompression.

587   Figure 10 is suggested to document the onset of coalescence of two bubbles. Decompression to a

588   lower P_{final} increased the available degassing time and therefore enhanced bubble growth by

589   expansion of the fluid phase, diffusion of H_2O into the bubbles and coalescence. The influence of

590   the degassing timescale is also apparent from the size of the bubbles at the capsule-melt interface

591   in the samples decompressed to 75 MPa. The bubbles in sample CD-C-3 (0.024 MPa·s^{-1}, Fig. 6,

592   eFigs. 2a and 2b) are clearly bigger than those in CD-C-4 (0.17 MPa·s^{-1}, Fig. 6, eFigs. 3a and 3b)

593   due to longer time for diffusive growth of heterogeneously nucleated bubbles at the capsule-melt

594   interface during decompression.

595   The big bubbles (up to 400 µm diameter) in the center of sample CD-C-3 are suggested to

596   have formed heterogeneously at low ΔP_{ss} at the capsule-melt interface on the bottom lid. After

26

597   detachment due to volume-related buoyancy force, these bubbles ascended during decompression

598   (Fig. 6, eFigs. 2a and 2b). Assuming heterogeneous nucleation at H_2O-saturated conditions (176

599   MPa for 4.7 wt% H_2O), it can be calculated from Equation 2 that a bubble with 400 µm diameter

600   already needs ~67 of the 69 minutes decompression time (0.024 MPa·s^{-1}) to ascent 4 mm in the

601   melt. Therefore, the ascent of the detached bubbles must have begun prior to homogeneous

602   nucleation. The ascending detached bubbles grew by volatile expansion and H_2O diffusion from

603   the supersaturated melt into the bubbles. The latter leads to depletion of H_2O in a spherical

604   drainage zone around the bubbles. Due to the ascent, the H_2O-depleted zone covers the whole

605   ascent track. This is evidenced by the absence of small homogeneously nucleated bubbles

606   (excerpt Fig. 6, eFigs. 2a and 2b) and lowered residual H_2O contents in the glass throughout the

607   tracks of the big detached bubbles. Homogeneous nucleation of the small bubbles therefore only

608   occurs in regions with higher H_2O supersaturation. Further ascent of the detached bubbles

609   through the melt might displace small homogeneously nucleated bubbles and can be accelerated

610   by growth due to coalescence and ripening processes. In the latter case, the detached bubbles

611   delete the nucleation history of an existing population by interaction with the smaller bubbles on

612   their ascent tracks and they may initiate the nucleation of a second bubble population during

613   further decompression in the depleted zones.

614   Both, the BSE and the TLM image of sample CD-C-4 (eFigs. 3a and 3b) shows that the lower

615   central part of the capsule contains more numerous and slightly bigger bubbles (~12 µm) than the

616   rest of the sample. In the case of homogeneous bubble nucleation, it is conceivable that the first

617   bubbles preferably nucleated in the lower central part of the sample and had more time to grow.

618   Mangan and Sisson (2000) observed a preferred bubble nucleation close to the upper capsule

619   headspace and attributed this effect to melt displacement during opening of the crimped capsule.

27

620   However, melt displacement at the bottom lid is unlikely for our capsule geometry. There is no

621   evidence that the shape of the capsule influences nucleation in our experiments.

622   The CI glass cylinder sample CD-C-5 with the lowest P_{final} of 60 MPa (0.17 MPa·s^{-1}) is the

623   most degassed cylinder sample with the highest porosity of ~10 % in the glass (Figs. 7a and 7b,

624   eFigs. 1a and 1b). Due to the lowest final P and the high N_V(n) with bubble diameters up to 13

625   μm, the corrected porosity (~25 %) in the melt is closer to the equilibrium porosity (~33 %) than

626   in samples decompressed to higher P_{final} of 75 and 100 MPa (Table 3). The N_V(n)-values of all

627   decompressed cylinder samples range within one order of magnitude ($6 \cdot 10^4 - 7 \cdot 10^5$ mm^{-3}) with a

628   conservatively estimated analytical error of half an order of magnitude based on the differences

629   in BSE and TLM measurements (Table 3). The high N_V(n)-value of the 60 MPa sample is a

630   further hint for homogeneous bubble nucleation in all cylinder samples. It is unlikely that bubbles

631   of up to 13 μm diameter grow during the few seconds of rapid quench. The size distribution (Fig.

632   7c) with a narrow size range of these bubbles documents a single nucleation event within a short

633   time interval as described in Figure 7b in Toramaru (1989). Considering homogeneous bubble

634   nucleation in the cylinder samples with a P_{final} of 100 MPa, we can estimate a ΔP_{HoN} of <76 MPa

635   for the CI and <70 MPa for the VAD79 melt using the solubility data of Fanara et al. (2015) and

636   Iacono Marziano et al. (2007), respectively.

637

638   **Integration of results into the model of Toramaru (2006)**

639   Toramaru (2006) reported a model to describe homogeneous nucleation and growth of

640   bubbles at a constant decompression rate. This formulation relates N_V(n) to physico-chemical

641   parameters such as surface tension, diffusivity and concentration of total H_2O (Eqn. 3).

$$N_V(n) = 34 \cdot C \cdot \left(\frac{16 \cdot \pi \cdot \sigma^3}{3 \cdot kT \cdot P_W^2} \right)^{-2} \cdot \left(\frac{V_m \cdot P_W}{kT} \right)^{-\frac{1}{4}} \cdot \left(\frac{P_W^2 \cdot kT \cdot C \cdot D}{4 \cdot \sigma^2 \cdot (dP/dt)} \right)^{-\frac{3}{2}} \qquad (3)$$

28

642   N_V(n) is the number of bubbles per unit of bubble-free melt volume (m^{-3}), C is the initial total

643   H_2O concentration expressed as molecular number per cubic meters (m^{-3}), σ is the surface

644   tension at the bubble-melt interface (N·m^{-1}), k is the Boltzmann constant (1.38·10^{-23} J·K^{-1}), T is

645   the temperature (K), P_W is the H_2O saturation pressure (Pa), V_m is the volume of a H_2O molecule

646   in the melt (3·10^{-29} m^3; Burnham and Davis, 1971), D is the total H_2O diffusivity in the silicate

647   melt (m^2·s^{-1}) and dP/dt is the decompression rate in Pa·s^{-1}. The conversion of N_V(t)- (e.g. provided

648   by the CSDCorrections software) into N_V(n) is essential, because only N_V(n)-values are

649   independent of diffusive bubble growth and expansion (Proussevitch et al., 2007; Toramaru,

650   1989).

651   This model is valid for homogeneous bubble nucleation in a melt free of pre-existing bubbles

652   during super-liquidus isothermal decompression at a constant rate in the diffusion-controlled

653   regime. The sample size has to be sufficient to guarantee a melt pool that is unaffected by

654   diffusional volatile loss to the capsule-melt interface. The application of this model necessitates a

655   completed single nucleation event as well as the absence of Ostwald ripening and coalescence.

656   The bubble size distribution should display a narrow size range and follow a linear trend in the ln

657    $n(l)$ vs. l plot, where $n(l)$ is the population density of bubbles with diameter l in a certain size

658   interval (Toramaru, 2006). The diffusion-controlled regime is defined by the parameter α_4 =

659    $t_{dec}P_W/4\eta > 2\cdot10^3$ (Toramaru, 1995), where t_{dec} is the time (s) needed for decompression to P_{final}.

660   For both melt compositions, α_4 is about 10^7 for a decompression rate of 0.17 MPa·s^{-1} and even

661   higher for lower decompression rates. However, during fast decompression to low P_{final} with

662   large ΔP, high-viscous melts such as rhyolites become viscosity-controlled, because the H_2O

663   content in the melt decreases due to exsolution while the viscosity steadily increases (cf. Fig. 9a

664   in Toramaru, 1995).

29

665   For exemplary purpose, the $N_V(n)$ of homogeneously nucleated bubbles of CI glass cylinder

666   experiments were applied to the model of Toramaru (2006). A surface tension of 0.133 N·m^{-1} was

667   derived from Bagdassarov et al. (2000) considering the dependence of total H_2O content and T on

668   σ. It has to be emphasized that the calculated surface tension of 0.133 N·m^{-1} is valid for rhyolitic

669   melts, not for compositions of samples in this study. In general, surface tension data by direct

670   measurement as described in Bagdassarov et al. (2000) are quite poor and unconstrained material

671   properties for compositions other than synthesized haplogranite. P_W for the H_2O content of 4.7

672   wt% at 1050 °C was extrapolated from the solubility experiments of Fanara et al. (2015) to be

673   ~176 MPa. The initial total H_2O content C of $3.54 \cdot 10^{27}$ m^{-3} was calculated using the melt density

674   at P_W and T provided by the model of Ochs and Lange (1999). The total H_2O diffusivity (D) of

675    $1.57 \cdot 10^{-10}$ m^2·s^{-1} was calculated for 1050 °C and 4.7 wt% H_2O by the formulation for trachytic

676   compositions given in Fanara et al. (2013). Application of Equation 3 results in calculated $N_V(n)$-

677   values that are up to five orders of magnitude lower than in the samples of our glass cylinder

678   experiments decompressed at rates of 0.024 and 0.17 MPa·s^{-1} to 100 - 60 MPa providing $N_V(n)$ of

679   ~10^5 mm^{-3} (Fig. 11). The same holds for VAD79 composition because the parameters D, C, σ, α_4

680   and P_W of Equation 3 are similar for the CI and the VAD79 melt.

681   The discrepancies between calculated and observed $N_V(n)$-values may be attributed to H_2O

682   species-related changes in C and D as well as the usage of a macroscopic surface tension. The

683   nucleation of bubbles is a process on a molecular scale, where macroscopic physical descriptions

684   are likely to fail (e.g. Bottinga and Javoy, 1990; Gonnermann and Gardner, 2013; Navon and

685   Lyakhovsky, 1998; Ruckenstein and Nowakowski, 1990; Sparks, 1978; Toramaru, 1989). Bubble

686   nucleation prerequisites the aggregation of H_2O molecule clusters with a typical critical radius of

687   1 – 10 nm (Gonnermann and Gardner, 2013; Toramaru, 1995) that is attributed to local

688   concentration fluctuations in the melt (Hurwitz and Navon, 1994). It is conceivable to refer the

30

689   coefficient C in Equation 3 to the actual concentration of H_2O molecules with respect to the

690   species concentrations of molecular H_2O and OH^- in the silicate melt at P-T conditions (Nowak

691   and Behrens, 1995; Nowak and Behrens, 2001). At a total H_2O content of 4.7 wt% and 1050 °C,

692   the molecular H_2O content is in the range of 1 wt%. Considering the H_2O speciation, D should be

693   substituted by the diffusivity of molecular H_2O (e.g. Toramaru, 1995), which is one order of

694   magnitude higher than the total H_2O diffusivity at experimental conditions (e.g. Behrens and

695   Nowak, 1997). Such an increase of D in Equation 3 results in a decrease of predicted $N_V(n)$ by

696   one order of magnitude (Fig. 11). In contrast, the decrease of C due to H_2O speciation barely

697   increases $N_V(n)$ by less than half an order of magnitude. In combination, these opposing effects

698   shift $N_V(n)$ to even lower values than necessary to describe our experimental data. In this model, a

699   significant increase of $N_V(n)$ can be achieved by decreasing the surface tension in Equation 3,

700   while using C and D for total H_2O. The best match of predicted $N_V(n)$ to our CI and VAD79

701   experimental results is achieved for a σ of ~0.003 N·m^{-1} (Fig. 11). Lowered surface tensions on

702   the molecular scale of bubble nucleation compared to macroscopic values were already suggested

703   in previous studies (e.g. Bottinga and Javoy, 1990; Gonnermann and Gardner, 2013; Hamada et

704   al., 2010; Kashchiev, 2003; Kashchiev, 2004; Ruckenstein and Nowakowski, 1990; Toramaru,

705   1990; Toramaru, 1995). This effect may be attributed to a dependence of surface tension on

706   bubble (nucleus) size (Ruckenstein and Nowakowski, 1990; Tolman, 1949), thermal fluctuations

707   supplying the energy of formation of a new surface (Bottinga and Javoy, 1990) or a diffuse

708   interface between nucleus and surrounding melt (Gonnermann and Gardner, 2013; Kashchiev,

709   2003; Kashchiev, 2004; Kelton and Greer, 2010). Actually, for the instantaneous decompression

710   experiments by Hurvitz and Navon (1994), Toramaru and Miwa (2008) argue that the $N_V(n)$ data

711   can be explained by using a very low effective σ of 0.016 N·m^{-1} with the number of nucleation

712   sites modifying the pre-exponential factor of the nucleation rate. However, a value of 0.003 N·m^{-1}

31

713   is significantly lower than any other suggested by bubble nucleation experiments and therefore

714   quite unlikely.

715   Navon and Lyakhovsky (1998) suggested a completely different approach to explain the

716   discrepancy between experimentally determined and modeled N_V(n). They proposed to consider

717   the diffusivity of silicate network components rather than H_2O diffusivity to form a H_2O bubble

718   nucleus in a hydrous supersaturated melt. This idea is based on the similar distances of

719   neighboring H_2O molecules in the fluid and in the melt, even if the species concentration of 1

720   wt% dissolved molecular H_2O is considered. At a P_{final} of 100 MPa, the calculated mean

721   distances are 0.6 nm in the fluid and 1.1 nm in the melt. The formation of a nucleus may

722   therefore be kinetically controlled by the diffusion of silicate network components to enable

723   clustering of H_2O molecules. In this case, the diffusivity of network forming cations linked to

724   melt viscosity becomes a controlling factor (Navon and Lyakhovsky, 1998). This relation can be

725   expressed by the equation of Eyring (1936):

$$D = \frac{kT}{\eta \cdot \lambda} \qquad\qquad (4)$$

726   where k is the Boltzmann constant, T the temperature in K, λ the jump distance in m and η the

727   viscosity in Pa·s. It is noteworthy that this equation is not exactly correct for silicate melts other

728   than a pure SiO_2 melt (Liang et al., 1996), but in first approximation the diffusivity of network

729   formers can be calculated. A mean jump distance of $3 \cdot 10^{-10}$ m for the chemical diffusivity of high

730   field strength elements like Zr^{4+} in both dry and hydrous melts was determined by Koepke and

731   Behrens (2001) and is suggested to be comparable to Si^{4+} and Al^{3+} diffusion. At 1050 °C and 4.7

732   wt% total H_2O a viscosity of 77 Pa·s was calculated using the relation of Misiti et al. (2011) for

733   the CI melt. Insertion of the jump distance into Equation 4 provides a network former diffusivity

734   of $8 \cdot 10^{-13}$ m²·s⁻¹ that is more than 2 orders of magnitude lower than the total H_2O diffusivity. The

735   corresponding shift of the $\log N_V(n)/(dP/dt)$ line in Fig. 11 by 3.5 orders of magnitude is still not

736   sufficient to match the experimentally determined $N_V(n)$. However, in combination with a

737   moderate reduction of the macroscopic surface tension from o value of 0.133 to 0.042 N·m^{-1} the

738   model of Toramaru (2006) can match the experimental data.

739   In addition, Fig. 11 shows a comparison between $N_V(n)$-values of this study and selected

740   data of previous studies (Gondé et al., 2011; Mangan and Sisson, 2000; Marxer et al., 2015;

741   Mourtada-Bonnefoi and Laporte, 2002). The presented $N_V(n)$ are obtained from pairs of

742   experiments with equal or at least comparable decompression rates that are characterized by low

743   and high ΔP (filled vs. open symbols). Experiments using glass powder as starting material were

744   not considered, because the observed $N_V(n)$ are mainly controlled by the number of hydration or

745   H_2O-N_2 bubbles in the melt prior to decompression. Samples with low ΔP close to the terminus

746   of the homogeneous nucleation event potentially fulfill the criteria for the application of the

747   vesiculation model of Toramaru (2006). A reliable experimentally determined $N_V(n)$ of Gondé et

748   al. (2011) for a haplogranitic melt representing the $N_V(n)$ directly after bubble nucleation (sample

749   #45 in Gondé et al., 2011; filled hexagon in Fig. 11) is three orders of magnitude higher than the

750   modeled value using the macroscopic σ and H_2O diffusivity. It is in the range of our determined

751     $N_V(n)$ and supports (1) the credibility of our results in terms of high $N_V(n)$ produced by

752   homogeneous bubble nucleation well above the liquidus, (2) that $N_V(n)$ is within error

753   independent of composition and (3) the suggestion of a reduced surface tension and/or the effect

754   of silicate network component diffusivity for the bubble nucleation process. This observation is

755   confirmed by high $N_V(n)$ values of decompressed hydrous rhyolitic melts reported in Mangan and

756   Sisson (2000) (sample #37) and Mourtada-Bonnefoi and Laporte (2002) (samples VGD33 and

757   VGD43) not influenced by bubble coalescence presented in Fig. 11 (filled symbols).

33

758   In contrast to samples quenched subsequently after the nucleation event, samples with higher

759   ΔP and identical/similar dP/dt (open symbols in Fig. 11) are mostly characterized by orders of

760   magnitude lower $N_V(n)$. Marxer et al. (2015) performed decompression experiments with the

761   VAD79 composition from 200 MPa down to a P_{final} of 75 MPa (CD18, CD19, CD21), but with a

762   higher initial H_2O content of ~5.2 wt% and still slightly H_2O-undersaturated at 200 MPa. Higher

763   initial H_2O content in the melt at otherwise identical conditions is equivalent to a higher bubble

764   nucleation P during decompression. In combination with a lower P_{final}, the timescale for bubble

765   coalescence that reduces $N_V(n)$ is extended. This is supported by the $N_V(n)$ of samples from

766   experiments with higher ΔP reported in Gondé et al. (2011) (sample #23), Mangan and Sisson

767   (2000) (sample #69) and Mourtada-Bonnefoi and Laporte (2002) (samples VGD59 and VGD31)

768   that are plotted in Fig. 11 (open symbols). Early bubble coalescence during decompression was

769   already observed by Mourtada-Bonnefoi and Laporte (2002) and in situ in HDAC experiments by

770   Gondé et al. (2011). Recent in situ observation of Masotta et al. (2014) have shown that massive

771   bubble coalescence can occur within minutes in nominally H_2O-free, highly viscous rhyodacitic

772   melts at 1100 °C and ambient P. The time interval for extensive bubble coalescence is expected

773   to be shortened down to a scale of seconds in case of less silicic, hydrous melts. This

774   consideration implies that the observed $N_V(n)$ are strongly dependent on the instant of time at

775   which the samples are quenched. This might be the explanation for the still high values of $N_V(n)$

776   of sample CD-C-5 (~4.7 wt% H_2O, 0.17 MPa·s^{-1}) decompressed to 60 MPa. It is conceivable that

777   this sample was quenched just before the onset of extensive bubble coalescence.

778   The $N_V(n)$ of the 5 mm samples in Marxer et al. (2015) are over the whole range of applied

779   decompression rates close to the values predicted by the model of Toramaru (2006) using the

780   total H_2O diffusivity and the macroscopic surface tension of 0.133 N·m^{-1} which does not apply to

781   our newly determined data. Among other studies, Toramaru (2006) used some $N_V(n)$ of

34

782   decompression experiments reported e.g. in Mangan and Sisson (2000) and Mourtada-Bonnefoi

783   and Laporte (2002) to adjust the model parameters. If these parameters are based on experiments

784   that were already subject to N_V(n) reduction, the modeled N_V(n) will also be underestimated. It

785   may therefore be necessary to improve current models for homogeneous bubble nucleation with

786   data from new experiments.

787

788   **Implications and limitations for future studies of homogeneous bubble nucleation in silicate**

789   **melts**

790   The prerequisite to study homogeneous bubble nucleation is a single-phase melt. As

791   documented in this study and in Marxer et al. (2015) this can be ensured by using massive glass

792   cylinders as starting material and sufficient t_{eq} to guarantee a homogeneous volatile content in the

793   melt prior to decompression. Further parameters such as volatile diffusivity, η and σ that are

794   dependent on melt composition and temperature should be considered before conducting

795   degassing experiments, because the investigation of homogeneous nucleation and growth of

796   volatile bubbles during isothermal decompression requires an experimental window, where the

797   experimental result is mainly controlled by the decompression path. An important limiting

798   parameter is the decompression timescale that is defined by the decompression rate and P_{final}. The

799   time-dependent diffusional loss of volatiles into heterogeneously nucleated bubbles at the

800   capsule-melt interface defines the minimum sample diameter needed to retain a sufficiently sized

801   unaffected melt pool in the center of the specimen. Furthermore, the decompression duration is

802   limited by the ascent of heterogeneously formed bubbles at the capsule-melt interface that is

803   dependent on melt viscosity. These two limitations require the largest technically possible

804   capsule dimensions. On the other hand, a bigger capsule volume leads to a decrease in cooling

805   rate and therefore to possible quench crystal formation. In order to study a single homogeneous

806   bubble nucleation event, P_{final} has to be as close to the terminus of the event as possible.

807   Unnecessary low P_{final} increase the degassing timescale and enable bubble growth by coalescence

808   that leads to a reduction of $N_V(n)$. Increasing porosities in the samples decrease the inter-bubble

809   distances and aggravate the interaction of bubbles. Additionally, high porosities cause massive

810   shrinkage of bubbles due to the significant decrease in molar volume of the fluid during isobaric

811   quench. This reduction of bubble volumes necessitates the correction of bubble sizes and

812   porosities that are determined from the vitrified samples in order to match the conditions prior to

813   quench (Marxer et al., 2015).

814   Considering these experimental limitations, future experiments will improve the investigation

815   of homogeneous bubble nucleation in silicate melts. This will contribute to a better understanding

816   of melt degassing triggering volcanic eruptions at the interface of the molecular to the

817   macroscopic world during magma ascent.

818

828

829   **References cited**

830 Appen, A.A. (1949) Berechnung der optischen Eigenschaften, der Dichte und des

831   Ausdehnungskoeffizienten von Silikatgläsern aus ihrer Zusammensetzung. Ber. Akad.

832   Wiss. UdSSR, 69, 841-844.

833 Bagdassarov, N., Dorfman, A., and Dingwell, D.B. (2000) Effect of alkalis, phosphorus, and

834   water on the surface tension of haplogranite melt. American Mineralogist, 85, 33-40.

835 Behrens, H., and Nowak, M. (1997) The mechanisms of water diffusion in polymerized silicate

836   melts. Contributions to Mineralogy and Petrology, 126, 377-385.

837 -. (2003) Quantification of H_2O speciation in silicate glasses and melts by IR spectroscopy - In

838   situ versus quench techniques. Phase Transitions, 76, 45-61.

839 Berlo, K., Gardner, J.E., and Blundy, J.D. (2011) Timescales of magma degassing. Timescales of

840   magmatic processes: From core to atmosphere, p. 231-255. John Wiley & Sons, Ltd.

841 Berndt, J., Liebske, C., Holtz, F., Freise, M., Nowak, M., Ziegenbein, D., Hurkuck, W., and

842   Koepke, J. (2002) A combined rapid-quench and H_2-membrane setup for internally heated

843   pressure vessels: Description and application for water solubility in basaltic melts.

844   American Mineralogist, 87, 1717-1726.

845 Bottinga, Y., and Javoy, M. (1990) MORB degassing: bubble nucleation. Journal of Geophysical

846   Ressearch, 95, 5125–5131.

847 Burnham, C.W., and Davis, N.F. (1971) The role of H_2O in silicate melts: 1. P-V-T relations in

848   the system $NaAlSi_3O_8$-H_2O to 10 kilobars and 1000 °C. American Journal of Science,

849   270, 54-79.

850 Carroll, M.R., and Webster, J.D. (1994) Solubilities of sulfur, noble gases, nitrogen, chlorine, and

851   fluorine in magmas. In P.H. Ribbe, Ed. Volatiles in Magmas, 30, p. 231-279. Reviews in

852   Mineralogy, Washington, DC.

37

853   Civetta, L., Orsi, G., Pappalardo, L., Fisher, R.V., Heiken, G., and Ort, M. (1997) Geochemical

854   zoning, mingling, eruptive dynamics and depositional processes - The Campanian

855   Ignimbrite, Campi Flegrei caldera, Italy. Journal of Volcanology and Geothermal

856   Research, 75, 183-219.

857   Davis, M.J., and Ihinger, P.D. (1998) Heterogeneous crystal nucleation on bubbles in silicate

858   melt. American Mineralogist, 83, 1008-1015.

859   De Vivo, B., Petrosino, P., Lima, A., Rolandi, G., and Belkin, H.E. (2010) Research progress in

860   volcanology in the Neapolitan area, southern Italy: a review and some alternative views.

861   Mineralogy and Petrology, 99, 1-28.

862   Dingwell, D.B., and Webb, S.L. (1990) Relaxation in silicate melts. European Journal of

863   Mineralogy, 2, 427-449.

864   Duan, Z., and Zhang, Z. (2006) Equation of state of the H_2O-CO_2 system up to 10 GPa and 2573

865   K: Molecular dynamics simulations with ab initio potential surface. Geochimica et

866   Cosmochimica Acta, 70, 2311-2324.

867   Eyring, H. (1936) Viscosity, plasticity, and diffusion as examples of absolute reaction rates.

868   Journal of Chemical Physics, 4, 283-291.

869   Fanara, S., Behrens, H., and Zhang, Y.X. (2013) Water diffusion in potassium-rich phonolitic

870   and trachytic melts. Chemical Geology, 346, 149-161.

871   Fanara, S., Botcharnikov, R.E., Husen, A., Buddensieck, J., and Behrens, H. (2012) Pre-eruptive

872   conditions of the Campanian Ignimbrite eruption: experimental constraints from phase

873   equilibria and volatile solubility studies. Proceedings of IODP-ICDP Kolloquium, p. 41-

874   43, Kiel, Germany.

38

875   Fanara, S., Botcharnikov, R.E., Palladino, D.M., Adams, F., Buddensieck, J., Mulch, A., and

876   Behrens, H. (2015) Volatiles in magmas related to the Campanian Ignimbrite eruption:

877   experiments vs. natural findings. American Mineralogist, 100, 2284-2297.

878   Fiege, A., Holtz, F., and Cichy, S.B. (2014) Bubble formation during decompression of andesitic

879   melts. American Mineralogist, 99, 1052-1062.

880   Gardner, J.E. (2007) Heterogeneous bubble nucleation in highly viscous silicate melts during

881   instantaneous decompression from high pressure. Chemical Geology, 236, 1-12.

882   Gardner, J.E., Hilton, M., and Carroll, M.R. (1999) Experimental constraints on degassing of

883   magma: isothermal bubble growth during continuous decompression from high pressure.

884   Earth and Planetary Science Letters, 168, 201-218.

885   Giordano, D., Russell, J.K., and Dingwell, D.B. (2008) Viscosity of magmatic liquids: A model.

886   Earth and Planetary Science Letters, 271, 123-134.

887   Gondé, C., Martel, C., Pichavant, M., and Bureau, H. (2011) In situ bubble vesiculation in silicic

888   magmas. American Mineralogist, 96, 111-124.

889   Gonnermann, H.M., and Gardner, J.E. (2013) Homogeneous bubble nucleation in rhyolitic melt:

890   Experiments and nonclassical theory. Geochemistry, Geophysics, Geosystems, 14, 4758-

891   4773.

892   Gonnermann, H.M., and Manga, M. (2007) The fluid mechanics inside a volcano. Annual

893   Review of Fluid Mechanics, 39, 321-356.

894   Hamada, M., Laporte, D., Cluzel, N., Koga, K.T., and Kawamoto, T. (2010) Simulating bubble

895   number density of rhyolitic pumices from Plinian eruptions: constraints from fast

896   decompression experiments. Bulletin of Volcanology, 72, 735-746.

897   Higgins, M.D. (2000) Measurement of crystal size distributions. American Mineralogist, 85,

898   1105-1116.

899   -. (2006) Verification of ideal semi-logarithmic, lognormal or fractal crystal size distributions

900   from 2D datasets. Journal of Volcanology and Geothermal Research, 154, 8-16.

901   Hirth, J.P., Pound, G.M., and Stpierre, G.R. (1970) Bubble nucleation. Metallurgical

902   Transactions, 1, 939-945.

903   Hurwitz, S., and Navon, O. (1994) Bubble nucleation in rhyolitic melts - experiments at high-

904   pressure, temperature, and water-content. Earth and Planetary Science Letters, 122, 267-

905   280.

906   Iacono Marziano, G., Schmidt, B.C., and Dolfi, D. (2007) Equilibrium and disequilibrium

907   degassing of a phonolitic melt (Vesuvius AD 79 "white pumice") simulated by

908   decompression experiments. Journal of Volcanology and Geothermal Research, 161, 151-

909   164.

910   Kashchiev, D. (2003) Thermodynamically consistent description of the work to form a nucleus of

911   any size. Journal of Chemical Physics, 118, 1837-1851.

912   -. (2004) Multicomponent nucleation: thermodynamically consistent description of the nucleation

913   work. Journal of Chemical Physics, 120, 3749-58.

914   Kawamoto, T., and Hirose, K. (1994) Au-Pd sample containers for melting experiments on iron

915   and water-bearing systems. European Journal of Mineralogy, 6, 381-385.

916   Kelton, K.F., and Greer, A.L. (2010) Nucleation in Condensed Matter: Applications in Materials

917   and Biology, 15, p. 726. Pergamon Materials Series, Oxford, UK.

918   Kloess, G.H. (2000) Dichtefluktuationen natu rlicher Gläser. Habilitation thesis. University of

919   Jena.

920   Koepke, J., and Behrens, H. (2001) Trace element diffusion in andesitic melts: An application of

921   synchrotron X-ray fluorescence analysis. Geochimica et Cosmochimica Acta, 65, 1481-

922   1498.

40

923   Larsen, J.F., and Gardner, J.E. (2000) Experimental constraints on bubble interactions in rhyolite

924   melts: implications for vesicle size distributions. Earth and Planetary Science Letters, 180,

925   201-214.

926   Liang, Y., Richter, F.M., Davis, A.M., and Watson E.B. (1996) Diffusion in silicate melts . 1.

927   Self diffusion in $CaO-Al_2O_3-SiO_2$ at 1500 °C and 1 GPa. Geochimica et Cosmochimica

928   Acta, 60, 4353-4367.

929   Libourel, G., Marty, B., and Humbert, F. (2003) Nitrogen solubility in basaltic melt. Part I. Effect

930   of oxygen fugacity. Geochimica et Cosmochimica Acta, 67, 4123-4135.

931   Mangan, M., and Sisson, T. (2000) Delayed, disequilibrium degassing in rhyolite magma:

932   decompression experiments and implications for explosive volcanism. Earth and

933   Planetary Science Letters, 183, 441-455.

934   Martel, C., and Iacono-Marziano, G. (2015) Timescales of bubble coalescence, outgassing, and

935   foam collapse in decompressed rhyolitic melts. Earth and Planetary Science Letters, 412,

936   173-185.

937   Marxer, H., Bellucci, P., and Nowak, M. (2015) Degassing of H_2O in a phonolitic melt: A closer

938   look at decompression experiments. Journal of Volcanology and Geothermal Research,

939   297, 109-124.

940   Masotta, M., Ni, H., and Keppler, H. (2014) In situ observations of bubble growth in basaltic,

941   andesitic and rhyodacitic melts. Contributions to Mineralogy and Petrology, 167, 976-

942   989.

943   Mastrolorenzo, G., and Pappalardo, L. (2006) Magma degassing and crystallization processes

944   during eruptions of high-risk Neapolitan-volcanoes: Evidence of common equilibrium

945   rising processes in alkaline magmas. Earth and Planetary Science Letters, 250, 164-181.

41

946   Misiti, V., Vetere, F., Freda, C., Scarlato, P., Behrens, H., Mangiacapra, A., and Dingwell, D.B.

947   (2011) A general viscosity model of Campi Flegrei (Italy) melts. Chemical Geology, 290,

948   50-59.

949   Miyazaki, A., Hiyagon, H., Sugiura, N., Hirose, K., and Takahashi, E. (2004) Solubilities of

950   nitrogen and noble gases in silicate melts under various oxygen fugacities: implications

951   for the origin and degassing history of nitrogen and noble gases in the earth. Geochimica

952   et Cosmochimica Acta, 68, 387-401.

953   Morizet, Y., Nichols, A.R.L., Kohn, S.C., Brooker, R.A., and Dingwell, D.B. (2007) The

954   influence of H_2O and CO_2 on the glass transition temperature: insights into the effects of

955   volatiles on magma viscosity. European Journal of Mineralogy, 19, 657-669.

956   Mourtada-Bonnefoi, C.C., and Laporte, D. (2002) Homogeneous bubble nucleation in rhyolitic

957   magmas: An experimental study of the effect of H_2O and CO_2. Journal of Geophysical

958   Research-Solid Earth, 107(B4), ECV 2-1–ECV 2-19.

959   Navon, O., and Lyakhovsky, V. (1998) Vesiculation processes in silicic magmas. Geological

960   Society, London, Special Publications, 145, 27-50.

961   Nowak, M., and Behrens, H. (1995) The speciation of water in haplogranitic glasses and melts

962   determined by in situ near-infrared spectroscopy. Geochimica et Cosmochimica Acta, 59,

963   3445-3450.

964   -. (1997) An experimental investigation on diffusion of water in haplogranitic melts.

965   Contributions to Mineralogy and Petrology, 126, 365-376.

966   -. (2001) Water in rhyolitic magmas: getting a grip on a slippery problem. Earth and Planetary

967   Science Letters, 184, 515-522.

968   Nowak, M., Cichy, S.B., Botcharnikov, R.E., Walker, N., and Hurkuck, W. (2011) A new type of

969   high-pressure low-flow metering valve for continuous decompression: First experimental

970   results on degassing of rhyodacitic melts. American Mineralogist, 96, 1373-1380.

971   Ochs, F.A., and Lange, R.A. (1999) The Density of Hydrous Magmatic Liquids. Science, 283,

972   1314-1317.

973   Ohlhorst, S., Behrens, H., and Holtz, F. (2001) Compositional dependence of molar absorptivities

974   of near-infrared OH^- and H_2O bands in rhyolitic to basaltic glasses. Chemical Geology,

975   174, 5-20.

976   Orsi, G., Dantonio, M., Devita, S., and Gallo, G. (1992) The Neapolitan Yellow Tuff, a large-

977   magnitude trachytic phreatoplinian eruption - eruptive dynamics, magma withdrawal and

978   caldera collapse. Journal of Volcanology and Geothermal Research, 53, 275-287.

979   Pappalardo, L., and Mastrolorenzo, G. (2012) Rapid differentiation in a sill-like magma

980   reservoir: a case study from the campi flegrei caldera. Science Reports, 2, 712.

981   Proussevitch, A.A., Sahagian, D.L., and Kutolin, A. (1993) Stability of foams in silicate melts.

982   Journal of Volcanology and Geothermal Research, 59, 161-178.

983   Proussevitch, A.A., Sahagian, D.L., and Tsentalovich, E.P. (2007) Statistical analysis of bubble

984   and crystal size distributions: Formulations and procedures. Journal of Volcanology and

985   Geothermal Research, 164, 95-111.

986   Rolandi, G., Bellucci, F., Heizler, M.T., Belkin, H.E., and De Vivo, B. (2003) Tectonic controls

987   on the genesis of ignimbrites from the Campanian Volcanic Zone, southern Italy.

988   Mineralogy and Petrology, 79, 3-31.

989   Roskosz, M., Bouhifd, M.A., Jephcoat, A.P., Marty, B., and Mysen, B.O. (2013) Nitrogen

990   solubility in molten metal and silicate at high pressure and temperature. Geochimica et

991   Cosmochimica Acta, 121, 15-28.

43

992   Ruckenstein, E., and Nowakowski, B. (1990) A kinetic-theory of nucleation in liquids. Journal of

993   Colloid and Interface Science, 137, 583-592.

994   Schneider, C.A., Rasband, W.S., and Eliceiri, K.W. (2012) NIH Image to ImageJ: 25 years of

995   image analysis. Nature Methods, 9, 671-675.

996   Scholze, H. (1960) Zur Frage der Unterscheidung zwischen H_2O-Molekülen und OH-Gruppen in

997   Gläsern und Mineralen. Naturwissenschaften, 47, 226 (in German).

998   Simakin, A.G., Armienti, P., and Epel'baum, M.B. (1999) Coupled degassing and crystallization:

999   experimental study at continuous pressure drop, with application to volcanic bombs.

1000   Bulletin of Volcanology, 61, 275-287.

1001   Sparks, R.S.J. (1978) The dynamics of bubble formation and growth in magmas: A review and

1002   analysis. Journal of Volcanology and Geothermal Research, 3, 1-37.

1003   Suzuki, Y., Gardner, J.E., and Larsen, J.F. (2007) Experimental constraints on syneruptive

1004   magma ascent related to the phreatomagmatic phase of the 2000 AD eruption of Usu

1005   volcano, Japan. Bulletin of Volcanology, 69, 423-444.

1006   Stelling, J., Botcharnikov, R.E., Beermann, O., and Nowak, M. (2008) Solubility of H_2O- and

1007   chlorine-bearing fluids in basaltic melt of Mount Etna at T=1050-1250°C and P=200

1008   MPa. Chemical Geology, 256, 102-110.

1009   Tolman, R.C. (1949) The effect of droplet size on surface tension. Journal of Chemical Physics,

1010   17, 333-337.

1011   Toramaru, A. (1989) Vesiculation process and bubble size distributions in ascending magmas

1012   with constant velocities. Journal of Geophysical Research: Solid Earth, 94(B12), 17523-

1013   17542.

44

1014   -. (1990) Measurement of bubble-size distributions in vesiculated rocks with implications for

1015   quantitative estimation of eruption processes. Journal of Volcanology and Geothermal

1016   Research, 43, 71-90.

1017   -. (1995) Numerical study of nucleation and growth of bubbles in viscous magmas. Journal of

1018   Geophysical Research: Solid Earth, 100, 1913-1931.

1019   -. (2006) BND (bubble number density) decompression rate meter for explosive volcanic

1020   eruptions. Journal of Volcanology and Geothermal Research, 154, 303-316.

1021   Toramaru, A., and Miwa, T. (2008) Vesiculation and crystallization under instantaneous

1022   decompression: Numerical study and comparison with laboratory experiments. Journal of

1023   Volcanology and Geothermal Research, 177, 983-996.

1024

1025 **Figure captions**

1026 **Figure 1.** TLM and BSE images of two CI isobaric experiments starting from glass cylinders

1027 with ~4.7 wt% H_2O, equilibrated for 96 h at 200 MPa and 1300 °C. (a) TLM image of IB-C-1b:

1028 RQ starting from 1300 °C. The glass section contains objects ≥1 μm diameter (black dots in

1029 focus plane) that are probably quench crystals. Some objects appear to be bigger in diameter due

1030 to the optical halo effect. (b) TLM image of IB-C-2: NQ starting from 1050 °C. The glass section

1031 contains quench crystal aggregates with radially arranged, needle-shaped crystals with several

1032 μm length. The quench crystals are bigger than in sample IB-C-1b due to the lower cooling rate.

1033 (c) BSE image of IB-C-2: Single quench crystal aggregate with needle-shaped crystals that are

1034 radially arranged around a central microlite of presumably different chemical composition. The

1035 crystals were too small for chemical analysis by EMP. The glass-crystal image contrast suggests

1036 an oxide microlite as central crystal in the aggregate.

1037

1038 **Figure 2.** Comparison of BSE images of selected samples decompressed to a P_{final} of 100 MPa

1039 (0.024 MPa·s^{-1}) using massive glass cylinders and powder with the CI and VAD79 composition

1040 as starting material. The orientation of the capsules during the runs was realized as displayed.

1041 Despite identical and homogeneous initial H_2O content in the melt prior to decompression, the

1042 glass powder samples that were equilibrated for a t_{eq} of 24 h (central row) are clearly more

1043 degassed than the samples starting from massive glass cylinders (top row) and glass powder with

1044 a t_{eq} of 96 h (bottom row). The powder samples with a t_{eq} of 24 h are characterized by bigger

1045 bubbles, higher porosities and lower bubble number densities. The bubbles in the samples with a

1046 t_{eq} of 96 h are only few μm in diameter, more numerous and homogeneously distributed in the

1047 glass. These small bubbles are not visible at this magnification.

1048

46

1049

1050   **Figure 3.** Comparison of BSE images of selected samples decompressed to a P_{final} of 100 MPa

1051   (0.17 MPa·s^{-1}) using a massive CI glass cylinder (t_{eq} = 96 h) and powder (t_{eq} = 24 h) as starting

1052   material. The top and the bottom of the images represent the orientation of the capsules during

1053   the decompression runs. In correspondence to the samples of the experiments with a lower

1054   decompression rate (shown in Fig. 2), the glass powder sample (CD-P-1, bottom image) is more

1055   degassed than the glass cylinder sample (CD-C-1, top image). The glass cylinder sample contains

1056   numerous small bubbles on a μm scale that are not visible at this magnification. The glass

1057   powder sample also features a belt of small bubbles in the central part of the capsule (right image

1058   excerpt).

1059

1060   **Figure 4.** TLM images of CI (two left images) and VAD79 (two right images) samples

1061   decompressed with 0.024 MPa·s^{-1} to a P_{final} of 100 MPa. All images have the same scale. The

1062   samples CD-C-2 (a) and CD-C-25 (c) started from glass cylinders and samples CD-P-2b (b) and

1063   CD-P-32 (d) from glass powder. All experiments were equilibrated for 96 h prior to

1064   decompression. All samples contain homogeneously distributed bubbles with few μm diameter.

1065   The N_V(n) and porosities of the samples are comparable for corresponding experiments with the

1066   same melt composition (see Table 3). In contrast to decompressed glass powder samples with a

1067 t_{eq} of 24 h, the degassing behavior of samples with a t_{eq} of 96 h is identical to the glass cylinder

1068   samples.

1069

1070   **Figure 5.** TLM images of CD-C-1 decompressed to a P_{final} of 100 MPa (0.17 MPa·s^{-1}) using a

1071   massive CI glass cylinder with different magnifications. The sample contains homogeneously

1072   distributed bubbles with several μm in diameter. The image reveals that some of these bubbles

47

1073   are in close vicinity to small opaque crystals, probably magnetite, and connected by a thin neck

1074   to the crystal surface. The formation of a thin neck towards a microlite is also described in

1075   Hurwitz and Navon (1994) and attributed to bubble shrinkage during quench.

1076

1077   **Figure 6.** BSE images of CI glass cylinder samples (CD-C-3, CD-C-4) decompressed to a P_{final}

1078   of 75 MPa with 0.024 MPa·s^{-1} (top image) and 0.17 MPa·s^{-1} (bottom image). The orientation of

1079   the capsules during the decompression runs are represented by the top and the bottom of the

1080   images. The area around each of the big bubbles in sample CD-C-3 is free of the elsewhere

1081   homogeneously distributed small bubbles with several µm in diameter (right image excerpt). For

1082   details see text.

1083

1084   **Figure 7.** BSE (a) and a mapped TLM image (b) of sample CD-C-5 decompressed to a P_{final} of

1085   60 MPa with 0.17 MPa·s^{-1}. The top and the bottom of the images represent the orientation of the

1086   capsules during the decompression runs. The TLM image reveals extensive convection patterns

1087   within the capsule. The bubbles in the BSE image were big enough to be analyzed with

1088   CSDCorrections software (Higgins, 2000). (c) Exemplary BSD plot derived from sample area 4

1089   in (a) shows the logarithmic population density ln $n(l)$ as a function of the diameter (l) of the

1090   bubbles in the quenched sample. The diameters correspond to the major axes of the bubble-

1091   ellipsoids. The BSD is characterized by a narrow size range and a near-linear trend.

1092

1093   **Figure 8.** H_2O-N_2 solubility model on the basis of the experimentally determined H_2O-CO_2

1094   solubility reported in Fanara et al. (in press) for the CI composition at the decompression T of

1095   1050 °C. The amounts of dissolved N_2 are maximum values as suggested by Carroll and Webster

1096   (1994). Isobars are adopted from Fanara et al. (in press) and are marked with the corresponding

48

1097   *P*. The dashed isopleth represents the fluid composition in equilibrium with the melt. At 200 MPa

1098   and an initial H_2O content of 4.7 wt% in the melt prior to decompression, the solubility of N_2 is

1099   correspondingly low. Thus, a significant amount of the N_2 in the capsule of glass powder samples

1100   remains in the H_2O-dominated fluid phase.

1101

1102   **Figure 9.** Ascent distance of H_2O bubbles as a function of bubble diameter for the equilibration

1103   and decompression *T* (1300 and 1050 °C) and two t_{eq}´s (24 and 96 h). Instant volatile saturation

1104   of the melt at the beginning of the equilibration period in the glass powder experiments is

1105   assumed. Increasing *T* accelerates bubble ascent due to the lowered viscosity of the melt and

1106   decreased density of the supercritical fluid (see text, Eqn. 2).

1107

1108   **Figure 10.** The TLM image of sample CD-C-4 decompressed to a P_{final} of 75 MPa with 0.17

1109 $MPa·s^{-1}$ shows two neighbored bubbles that extend towards each other by a small bulge. These

1110   bubbles were quenched just at the beginning of coalescence.

1111

1112   **Figure 11.** Logarithmic $N_V(n)$-values of samples of this study (error about ±0.5 log units) and of

1113   selected previous experimental studies as a function of decompression rate in comparison to the

1114   calculated $N_V(n)$-values for the CI melt using the model of Toramaru (2006). The trends were

1115   calculated (1) for a macroscopic surface tension of 0.133 $N·m^{-1}$ and a total H_2O diffusivity of

1116 $1.57·10^{-10}$ $m^2·s^{-1}$ (solid line) and (2) a network former diffusivity of $8·10^{-13}$ $m^2·s^{-1}$ in combination

1117   with a moderately lowered surface tension of 0.042 $N·m^{-1}$ (dashed line). Filled symbols represent

1118 $N_V(n)$ of samples from experiments where most likely coalescence did not occur. Empty symbols

1119   represent $N_V(n)$ of samples from experiments that are suggested to be influenced by coalescence

1120   reducing $N_V(n)$ (indicated by arrows). *Note*: Ma15: CD experiments of Marxer et al. (2015) in 5

49

1121   mm capsules, VAD79 composition at 1050 °C. Go11: TIHPV experiments of Gondé et al.

1122   (2011), haplogranite at 900°C. ML02: Mourtada-Bonnefoi and Laporte (2002), rhyolite at 800

1123   °C. MS00: Mangan and Sisson (2000), rhyolite at 900 °C.

1124

1125   **Electronic Appendix**

1126   **eFigure 1a.** BSE image of the CI glass cylinder sample CD-C-5 with a t_{eq} of 96 h and

1127   decompressed to a P_{final} of 60 MPa with 0.17 MPa·s^{-1}.

1128

1129   **eFigure 1b.** Mapped TLM image of the CI glass cylinder sample CD-C-5 with a t_{eq} of 96 h and

1130   decompressed to a P_{final} of 60 MPa with 0.17 MPa·s^{-1}.

1131

1132   **eFigure 2a.** BSE image of the CI glass cylinder sample CD-C-3 with a t_{eq} of 96 h and

1133   decompressed to a P_{final} of 75 MPa with 0.024 MPa·s^{-1}.

1134

1135   **eFigure 2b.** Mapped TLM image of the CI glass cylinder sample CD-C-3 with a t_{eq} of 96 h and

1136   decompressed to a P_{final} of 75 MPa with 0.024 MPa·s^{-1}.

1137

1138   **eFigure 3a.** BSE image of the CI glass cylinder sample CD-C-4 with a t_{eq} of 96 h and

1139   decompressed to a P_{final} of 75 MPa with 0.17 MPa·s^{-1}.

1140

1141   **eFigure 3b.** Mapped TLM image of the CI glass cylinder sample CD-C-4 with a t_{eq} of 96 h and

1142   decompressed to a P_{final} of 75 MPa with 0.17 MPa·s^{-1}.

1143

50

1144   **eFigure 4.** BSE image of the CI glass cylinder sample CD-C-1 with a t_{eq} of 96 h and

1145   decompressed to a P_{final} of 100 MPa with 0.17 MPa·s^{-1}.

1146

1147   **eFigure 5a.** BSE image of the CI glass powder sample CD-P-1 with a t_{eq} of 24 h and

1148   decompressed to a P_{final} of 100 MPa with 0.17 MPa·s^{-1}.

1149

1150   **eFigure 5b.** Mapped TLM image of the CI glass powder sample CD-P-1 with a t_{eq} of 24 h and

1151   decompressed to a P_{final} of 100 MPa with 0.17 MPa·s^{-1}.

1152

1153   **eFigure 6.** BSE image of the CI glass cylinder sample CD-C-2 with a t_{eq} of 96 h and

1154   decompressed to a P_{final} of 100 MPa with 0.024 MPa·s^{-1}.

1155

1156   **eFigure 7a.** BSE image of the CI glass powder sample CD-P-2a with a t_{eq} of 24 h and

1157   decompressed to a P_{final} of 100 MPa with 0.024 MPa·s^{-1}.

1158

1159   **eFigure 7b.** Mapped TLM image of the CI glass powder sample CD-P-2a with a t_{eq} of 24 h and

1160   decompressed to a P_{final} of 100 MPa with 0.024 MPa·s^{-1}.

1161

1162   **eFigure 8.** BSE image of the CI glass powder sample CD-P-2b with a t_{eq} of 96 h and

1163   decompressed to a P_{final} of 100 MPa with 0.024 MPa·s^{-1}.

1164

1165   **eFigure 9a.** BSE image of the VAD79 glass powder sample CD-P-22 with a t_{eq} of 24 h and

1166   decompressed to a P_{final} of 100 MPa with 0.024 MPa·s^{-1}.

1167

1168   **eFigure 9b.** Mapped TLM image of the VAD79 glass powder sample CD-P-22 with a t_{eq} of 24 h

1169   and decompressed to a P_{final} of 100 MPa with 0.024 MPa·s^{-1}.

1170

1171   **eFigure 10.** BSE image of the VAD79 glass cylinder sample CD-C-23 with a t_{eq} of 96 h and

1172   decompressed to a P_{final} of 100 MPa with 0.17 MPa·s^{-1}.

1173

1174   **eFigure 11a.** BSE image of the VAD79 glass powder sample CD-P-24 with a t_{eq} of 24 h and

1175   decompressed to a P_{final} of 100 MPa with 0.17 MPa·s^{-1}.

1176

1177   **eFigure 11b.** Mapped TLM image of the VAD79 glass powder sample CD-P-24 with a t_{eq} of 24

1178   h and decompressed to a P_{final} of 100 MPa with 0.17 MPa·s^{-1}.

1179

1180   **eFigure 12.** BSE image of the VAD79 glass cylinder sample CD-C-25 with a t_{eq} of 96 h and

1181   decompressed to a P_{final} of 100 MPa with 0.024 MPa·s^{-1}.

1182

1183   **eFigure 13.** BSE image of the VAD79 glass powder sample CD-P-32 with a t_{eq} of 96 h and

1184   decompressed to a P_{final} of 60 MPa with 0.17 MPa·s^{-1}.

1185

	CI	CI	VAD79	VAD79
	Civetta	**this study**	**Iacono Marziano**	**this study**
	XRF Data	**n = 27**	**n = 12**	**n = 17**
SiO$_2$	58.52	58.87 (34)	57.15 (39)	57.53 (63)
TiO$_2$	0.45	0.44 (2)	0.30 (5)	0.29 (2)
Al$_2$O$_3$	18.81	18.53 (23)	21.34 (25)	20.52 (18)
FeO[a]	4.36	4.41 (25)	2.70 (17)	2.71 (19)
MnO	0.08	0.08 (3)	0.14 (6)	0.14 (3)
MgO	1.48	1.42 (7)	0.39 (5)	0.38 (3)
CaO	4.13	4.09 (15)	3.26 (12)	3.32 (11)
Na$_2$O	2.92	3.08 (14)	5.16 (15)	5.38 (17)
K$_2$O	8.98	8.82 (16)	9.46 (15)	9.53 (21)
P$_2$O$_5$	0.26	0.25 (4)	0.09 (4)	0.10 (3)

Table 1. Chemical compositions (wt%, normalized to 100 %) of synthesized starting glasses based on analyses of natural CF Triflisco OP17c1-sp by XRF in Civetta et al. (1997) and natural VAD79 in Iacono Marziano et al. (2007).

Notes: Errors are provided in parentheses.

Standard deviation (1σ) based on EMPA analysis.

[a]: Total Fe concentration in the glass given as FeO.

1186

1187

Table 2. Run conditions and H_2O contents of isobaric experiments.

exp. #	composition	starting material	t_{eq}	quench method	T prior quench	weighed portion of H_2O in capsule	total H_2O content in glass by FTIR	number of analyzed objects	average object size	$N_C(t)$ (glass)[d]
		[h]			[°C]	[wt%][a]	[wt%][b]		[µm]	[mm^{-3}]
IB-C-1a	CI	cylinder	96	RQ	1050	4.75(0.05)	4.87(0.10)	82	0.3 - 1	1.17E+05
IB-C-1b	CI	cylinder	96	RQ	1300	4.73(0.05)	4.93(0.10)	84	0.7	1.11E+05
IB-C-2	CI	cylinder	96	NQ	1050	4.72(0.05)	4.66(0.10)	267	10 - 13	7.01E+04
REF12[c]	VAD79	cylinder	96	RQ	1050	4.86(0.05)	4.89(0.12)			
IB-P-1	CI	powder	24	RQ	1300	0.98(0.05)	1.10(0.05)			
IB-P-2	CI	powder	24	RQ	1300	1.95(0.05)	2.05(0.04)			
IB-P-3	CI	powder	24	RQ	1300	3.87(0.05)	4.01(0.13)			
IB-P-4	CI	powder	24	RQ	1300	4.76(0.05)	4.84(0.17)	280	0.3 - 1	4.42E+05

Equilibration temperature was 1300 °C and equilibration pressure was 200 MPa.

[a]: Weighing error in brackets.

[b]: Means of at least 10 individual measurements over the whole sample (±1σ in brackets), molar absorption coefficients and densities are provided in the text. Thickness of the samples ranges between 120 – 160 µm.

[c]: VAD79 composition, equilibrated at 1050°C, for details see Tab. 1 in Marxer et al. (2015).

[d]: $N_C(t)$ is the number of quench crystal aggregates per total unit volume derived from TLM.

1188

1189

Table 3. Synopsis of the decompression experiments and the main results.

exp. #	composition	starting material	t_{eq} [h]	P_{final} [MPa]	$dP \cdot dt^{-1}$ [MPa·s^{-1}]	total H$_2$O content dissolved in melt at P_{start} [wt%][a]	residual total H$_2$O content in glass by FTIR [wt%][b]	counting method	number of analyzed objects	average object size [μm]	2D porosity (glass) ImageJ [area%][c]	3D porosity (glass) from BSE or TLM [vol%]	equilibrium porosity (melt) [vol%][d]	expected porosity (melt) [vol%][e]	corrected porosity (melt) [vol%][f]	N_V(t) (glass) [mm^{-3}][g]	N_V(n) (melt) [mm^{-3}][h]	B_s[i]	comments
CD-C-5	CI	cylinder	96	60	0.17	4.78(5)	n.d.	BSE	430	7 - 9	8.59	8.88	33.6	n.d.	22.6	5.68E+05	6.23E+05	3.00	area 1
								BSE	453	7 - 9	10.36	10.5	33.6	n.d.	26.0	7.51E+05	8.39E+05	3.00	area 2
								BSE	441	7 - 9	8.66	9.09	33.6	n.d.	23.1	7.06E+05	7.77E+05	3.00	area 3
								BSE	438	7 - 9	10.9	10.9	33.6	n.d.	26.8	6.09E+05	6.84E+05	3.00	area 4
								BSE	440	7 - 9	9.63	9.84	33.6	n.d.	24.7	6.59E+05	7.30E+05	3.00	average
CD-C-3	CI	cylinder	96	75	0.024	4.78 (5)	4.57 (6)[j]	BSE	645	-	4.8	5.4	26.5	3.8	15.2	1.87E+05	1.98E+05	3.15	
								TLM	143	11.5 (2.0)		1.61	26.5	3.8	4.9	5.53E+04	5.62E+04	3.15	
CD-C-4	CI	cylinder	96	75	0.17	4.75 (5)	4.88 (13)[j]	BSE	507	-	3.3	3.6 (4)	26.2	0.0	10.5	6.12E+04	6.35E+04	3.15	
								TLM	182	~ 4		0.27	26.2	0.0	0.9	8.11E+04	7.55E+04	3.15	
CD-C-1	CI	cylinder	96	100	0.17	4.62 (5)	4.64 (10)[j]	TLM	529	4 - 5		0.54	14.0	0.0	1.6	1.52E+05	1.53E+05	2.98	
CD-P-1	CI	powder	24	100	0.17	4.67 (5)	4.06 (10)	BSE	123	-	4.8	4.9	14.5	8.0	13.3	204	215	2.98	area of big bubbles
								TLM	213	5 - 7		2.9	14.5	1.8	8.2	2.58E+05	2.64E+05	2.98	area of small bubbles
CD-C-2	CI	cylinder	96	100	0.024	4.68 (5)	4.58 (6)[j]	TLM	901	4 - 5		0.26	14.6	1.4	0.8	4.68E+05	4.69E+05	2.98	
CD-P-2a	CI	powder	24	100	0.024	4.74 (5)	3.81(8)	BSE	84	130	5.6	5.4 (1.5)	15.4	11.9	14.5	73	87	2.98	
CD-P-2b	CI	powder	96	100	0.024	4.64 (5)	4.73 (14)	TLM	218	1 - 2		0.1	14.2	0.0	0.3	2.73E+05	3.24E+05	2.98	
CD-P-22	VAD79	powder	24	100	0.024	4.73 (5)	3.71 (9)	BSE	229	-	4.5	6.1 (1.2)	15.1	12.9	13.6	508	541	2.51	
CD-C-23	VAD79	cylinder	96	100	0.17	4.76 (5)	4.83 (6)[j]	TLM	362	1 - 2		0.0	15.4	0.0	0.1	1.01E+05	1.01E+05	2.51	
CD-P-24	VAD79	powder	24	100	0.17	4.73 (5)	3.86 (4)	BSE	134	-	5.6	5.6 (8)	15.1	11.2	12.6	319	338	2.51	
CD-C-25	VAD79	cylinder	96	100	0.024	4.66 (5)	4.68 (5)[j]	TLM	493	1 - 2		0.05	14.4	0.0	0.1	1.29E+05	1.30E+05	2.51	
CD-P-32	VAD79	powder	96	100	0.024	4.73 (5)	4.60 (8)	TLM	156	1 - 2		0.07	15.1	1.8	0.2	1.77E+05	1.77E+05	2.51	

Starting pressure (P_{start}) was 200 MPa for all experiments.
[a]: Weighed portions of H$_2$O (weighing error in brackets).
[b]: Means of individual measurements in the center area of the sample (±1σ in brackets).
[c]: Porosity displayed as 2D phase proportion of bubbles determined from a representative excerpt in the sample center acquired by BSE imaging.
[d]: Calculated from Eq. 5 in Gardner et al. (1999) using solubility data of Fanara et al. (in press) and Iacono-Marziano et al. (2007).
[e]: Calculated from Eq. 5 in Gardner et al. (1999) using the residual H$_2$O contents.
[f]: Calculated from Eq. 3 in Marxer et al. (2015) using the corresponding shrinkage factor B_S and the 3D porosity.
[g]: N_V(t) is the number of bubbles per total unit volume ($V_{glass} + V_{bubbles}$).
[h]: N_V(n) is the number of bubbles normalized to the bubble-free volume.
[i]: Shrinkage factor calculated from Eq. 2 in Marxer et al. (2015).
[j]: Numerous small objects in the measuring volume.

	CI Civetta XRF Data	CI this study n = 27	VAD79 Iacono Marziano n = 12	VAD79 this study n = 17
Table 1		Chemical compositions (wt%, normalized to 100 %) of synthesized starting glasses based on analyses of natural CF Triflisco OP17c1-sp by XRF in Civetta et al. (1997) and natural VAD79 in Iacono Marziano et al. (2007).		

	CI **Civetta** **XRF Data**	**CI** **this study** **n = 27**	**VAD79** **Iacono Marziano** **n = 12**	**VAD79** **this study** **n = 17**
SiO$_2$	58.52	58.87 (34)	57.15 (39)	57.53 (63)
TiO$_2$	0.45	0.44 (2)	0.30 (5)	0.29 (2)
Al$_2$O$_3$	18.81	18.53 (23)	21.34 (25)	20.52 (18)
FeO[a]	4.36	4.41 (25)	2.70 (17)	2.71 (19)
MnO	0.08	0.08 (3)	0.14 (6)	0.14 (3)
MgO	1.48	1.42 (7)	0.39 (5)	0.38 (3)
CaO	4.13	4.09 (15)	3.26 (12)	3.32 (11)
Na$_2$O	2.92	3.08 (14)	5.16 (15)	5.38 (17)
K$_2$O	8.98	8.82 (16)	9.46 (15)	9.53 (21)
P$_2$O$_5$	0.26	0.25 (4)	0.09 (4)	0.10 (3)

Notes: Errors are provided in parentheses.

Standard deviation (1σ) based on EMPA analysis.

[a]: Total Fe concentration in the glass given as FeO.

Table 2 – Run conditions and H_2O contents of isobaric experiments.

exp. #	composition	starting material	t_{eq}	quench method	T prior quench	weighed portion of H_2O in capsule	total H_2O content in glass by FTIR	number of analyzed objects	average object size
			[h]		[°C]	[wt%][a]	[wt%][b]		[μm]
IB-C-1a	CI	cylinder	96	RQ	1050	4.75(0.05)	4.87(0.10)	82	0.3 - 1
IB-C-1b	CI	cylinder	96	RQ	1300	4.73(0.05)	4.93(0.10)	84	0.7
IB-C-2	CI	cylinder	96	NQ	1050	4.72(0.05)	4.66(0.10)	267	10 - 13
REF12[c]	VAD79	cylinder	96	RQ	1050	4.86(0.05)	4.89(0.12)		
IB-P-1	CI	powder	24	RQ	1300	0.98(0.05)	1.10(0.05)		
IB-P-2	CI	powder	24	RQ	1300	1.95(0.05)	2.05(0.04)		
IB-P-3	CI	powder	24	RQ	1300	3.87(0.05)	4.01(0.13)		
IB-P-4	CI	powder	24	RQ	1300	4.76(0.05)	4.84(0.17)	280	0.3 - 1

Equilibration temperature was 1300 °C and equilibration pressure was 200 MPa.

[a]:Weighing error in brackets.

[b]: Means of at least 10 individual measurements over the whole sample (±1σ in brackets), molar absorption coefficients and densities are provid
Thickness of the samples ranges between 120 – 160 μm.

[c]: VAD79 composition, equilibrated at 1050°C, for details see Tab. 1 in Marxer et al. (2015).

[d]: N_C(t) is the number of quench crystal aggregates per total unit volume derived from TLM.

$N_C(t)$ (glass)[d] [mm^{-3}]
1.17E+05
1.11E+05
7.01E+04
4.42E+05

led in the text.

Table 3 – Synopsis of the decompression experiments and the main results.

exp. #	composition	starting material	t_{eq} [h]	P_{final} [MPa]	$dP \cdot dt^{-1}$ [MPa·s⁻¹]	total H_2O content dissolved in melt at P_{start} [wt%][a]	residual total H_2O content in glass by FTIR [wt%][b]	counting method	number of analyzed objects
CD-C-5	CI	cylinder	96	60	0.17	4.78(5)	n.d.	BSE	430
								BSE	453
								BSE	441
								BSE	438
								BSE	440
CD-C-3	CI	cylinder	96	75	0.024	4.78 (5)	4.57 (6)[j]	BSE	645
								TLM	143
CD-C-4	CI	cylinder	96	75	0.17	4.75 (5)	4.88 (13)[j]	BSE	507
								TLM	182
CD-C-1	CI	cylinder	96	100	0.17	4.62 (5)	4.64 (10)[j]	TLM	529
CD-P-1	CI	powder	24	100	0.17	4.67 (5)	4.06 (10)	BSE	123
								TLM	213
CD-C-2	CI	cylinder	96	100	0.024	4.68 (5)	4.58 (6)[j]	TLM	901
CD-P-2a	CI	powder	24	100	0.024	4.74 (5)	3.81(8)	BSE	84
CD-P-2b	CI	powder	96	100	0.024	4.64 (5)	4.73 (14)	TLM	218
CD-P-22	VAD79	powder	24	100	0.024	4.73 (5)	3.71 (9)	BSE	229
CD-C-23	VAD79	cylinder	96	100	0.17	4.76 (5)	4.83 (6)[j]	TLM	362
CD-P-24	VAD79	powder	24	100	0.17	4.73 (5)	3.86 (4)	BSE	134

| **CD-C-25** | VAD79 | cylinder | 96 | 100 | 0.024 | 4.66 (5) | 4.68 (5)[j] | TLM | 493 |
| **CD-P-32** | VAD79 | powder | 96 | 100 | 0.024 | 4.73 (5) | 4.60 (8) | TLM | 156 |

Starting pressure (P_{start}) was 200 MPa for all experiments.

[a]: Weighed portions of H_2O (weighing error in brackets).

[b]: Means of individual measurements in the center area of the sample ($\pm 1\sigma$ in brackets).

[c]: Porosity displayed as 2D phase proportion of bubbles determined from a representative excerpt in the sample center acquired by BSE imaging.

[d]: Calculated from Eq. 5 in Gardner et al. (1999) using solubility data of Fanara et al. (in press) and Iacono-Marziano et al. (2007).

[e]: Calculated from Eq. 5 in Gardner et al. (1999) using the residual H_2O contents.

[f]: Calculated from Eq. 3 in Marxer et al. (2015) using the corresponding shrinkage factor B_S and the 3D porosity.

[g]: N_V(t) is the number of bubbles per total unit volume ($V_{glass} + V_{bubbles}$).

[h]: N_V(n) is the number of bubbles normalized to the bubble-free volume.

[i]: Shrinkage factor calculated from Eq. 2 in Marxer et al. (2015).

[j]: Numerous small objects in the measuring volume.

average object size [μm]	2D porosity (glass) ImageJ [area%][c]	3D porosity (glass) from BSE or TLM [vol%]	equilibrium porosity (melt) [vol%][d]	expected porosity (melt) [vol%][e]	corrected porosity (melt) [vol%][f]	$N_V(t)$ (glass) [mm^{-3}][g]	$N_V(n)$ (melt) [mm^{-3}][h]	B_s[i]	comments
7 - 9	8.59	8.88	33.6	n.d.	22.6	5.68E+05	6.23E+05	3.00	area 1
7 - 9	10.36	10.5	33.6	n.d.	26.0	7.51E+05	8.39E+05	3.00	area 2
7 - 9	8.66	9.09	33.6	n.d.	23.1	7.06E+05	7.77E+05	3.00	area 3
7 - 9	10.9	10.9	33.6	n.d.	26.8	6.09E+05	6.84E+05	3.00	area 4
7 - 9	9.63	9.84	33.6	n.d.	24.7	6.59E+05	7.30E+05	3.00	average
-	4.8	5.4	26.5	3.8	15.2	1.87E+05	1.98E+05	3.15	
11.5 (2.0)		1.61	26.5	3.8	4.9	5.53E+04	5.62E+04	3.15	
-	3.3	3.6 (4)	26.2	0.0	10.5	6.12E+04	6.35E+04	3.15	
~4		0.27	26.2	0.0	0.9	8.11E+04	7.55E+04	3.15	
4 - 5		0.54	14.0	0.0	1.6	1.52E+05	1.53E+05	2.98	
-	4.8	4.9	14.5	8.0	13.3	204	215	2.98	
5 - 7		2.9	14.5	1.8	8.2	2.58E+05	2.64E+05	2.98	area of big bubbles
4 - 5		0.26	14.6	1.4	0.8	4.68E+05	4.69E+05	2.98	area of small bubbles
130	5.6	5.4 (1.5)	15.4	11.9	14.5	73	87	2.98	
1 - 2		0.1	14.2	0.0	0.3	2.73E+05	3.24E+05	2.98	
-	4.5	6.1 (1.2)	15.1	12.9	13.6	508	541	2.51	
1 - 2		0.0	15.4	0.0	0.1	1.01E+05	1.01E+05	2.51	
-	5.6	5.6 (8)	15.1	11.2	12.6	319	338	2.51	

| 1 - 2 | 0.05 | 14.4 | 0.0 | 0.1 | 1.29E+05 | 1.30E+05 | 2.51 |
| 1 - 2 | 0.07 | 15.1 | 1.8 | 0.2 | 1.77E+05 | 1.77E+05 | 2.51 |

Figure 1

(a) IB-C-1b RQ — in focus — 10μm
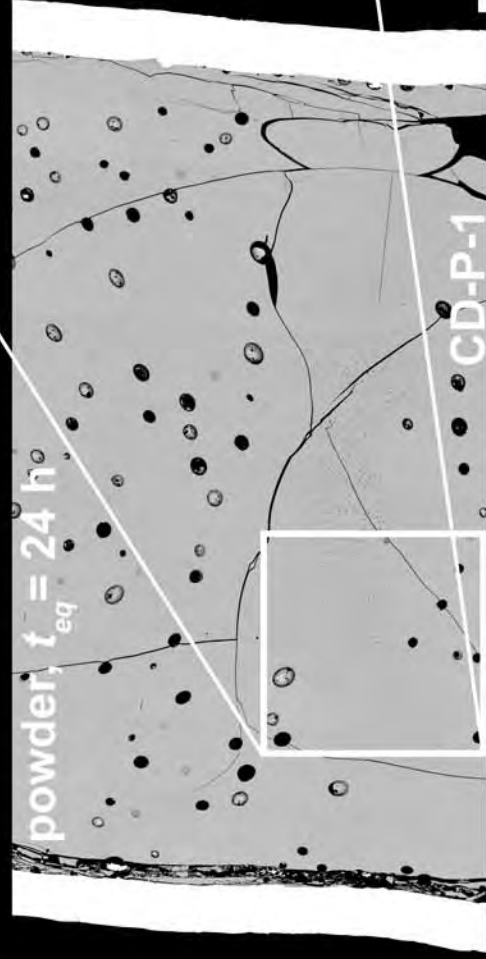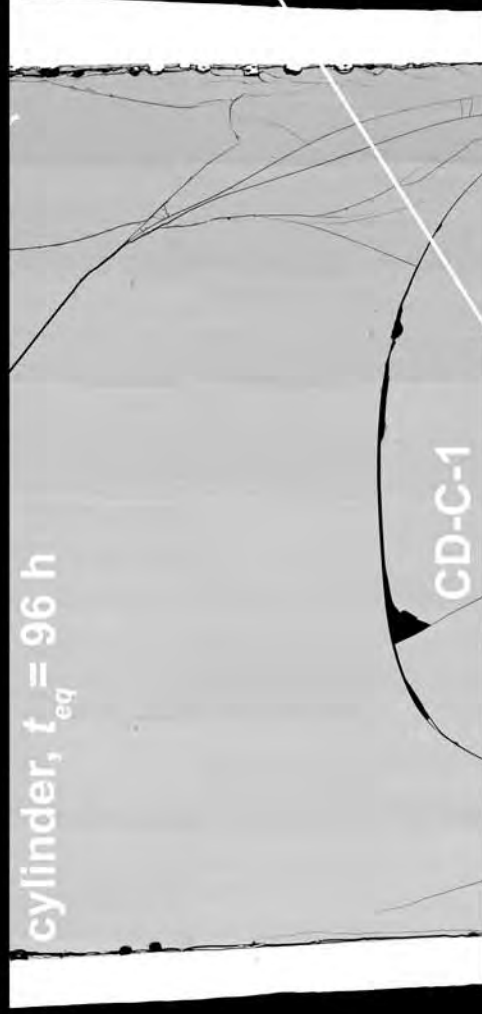(b) IB-C-2 NQ — 10μm
(c) IB-C-2 NQ — 1μm
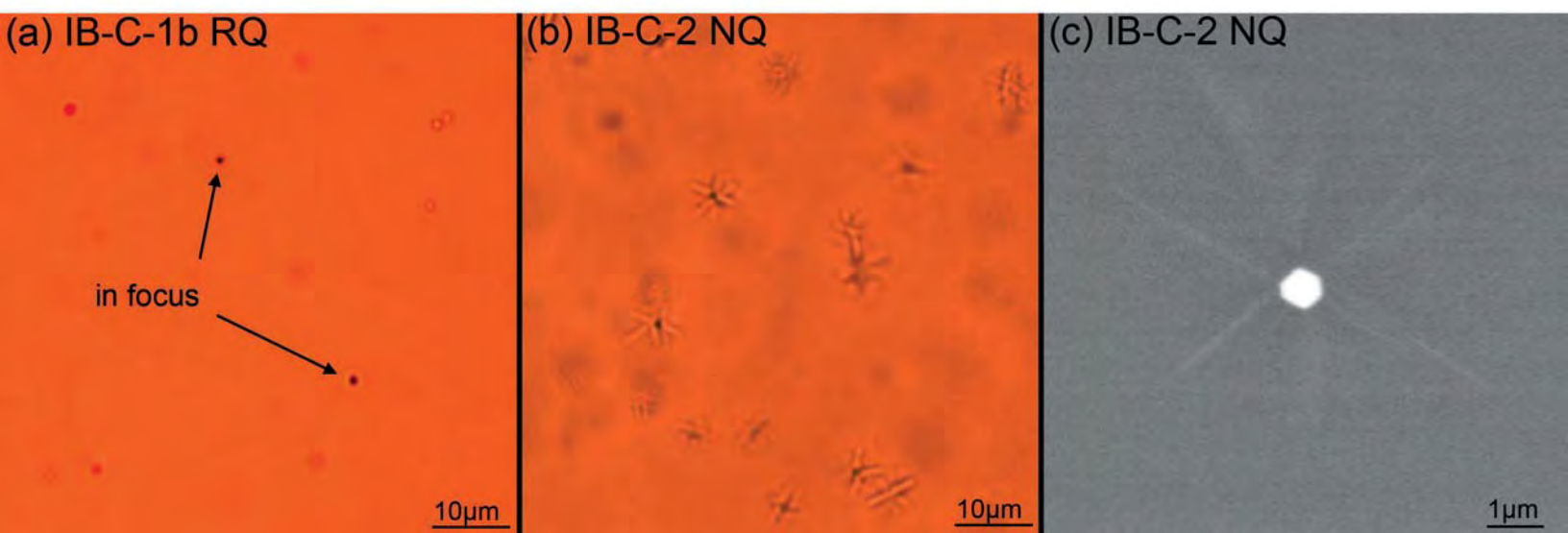
Figure 2

Campanian Ignimbrite (CI)

Vesuvius AD79

cylinder, t_{eq} = 96 h

CD-C-2

cylinder, t_{eq} = 96 h

CD-C-25

powder, t_{eq} = 24 h

CD-P-2a
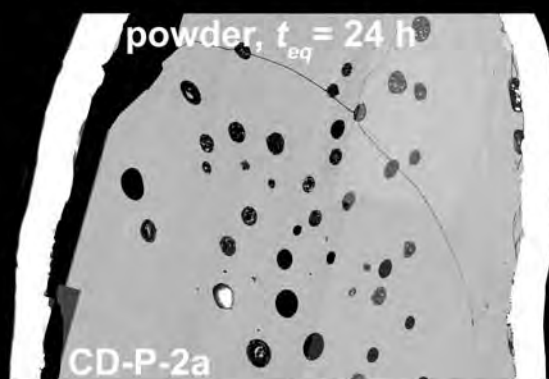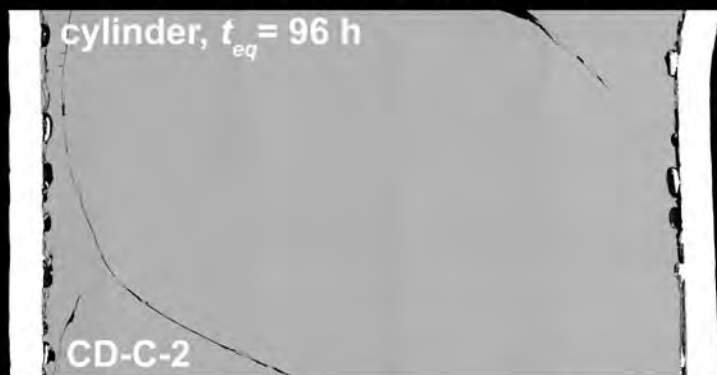
P_{final} = 100 MPa
0.024 MPa·s^{-1}

powder, t_{eq} = 24 h

CD-P-22

powder, t_{eq} = 96 h

CD-P-2b

powder, t_{eq} = 96 h

CD-P-32
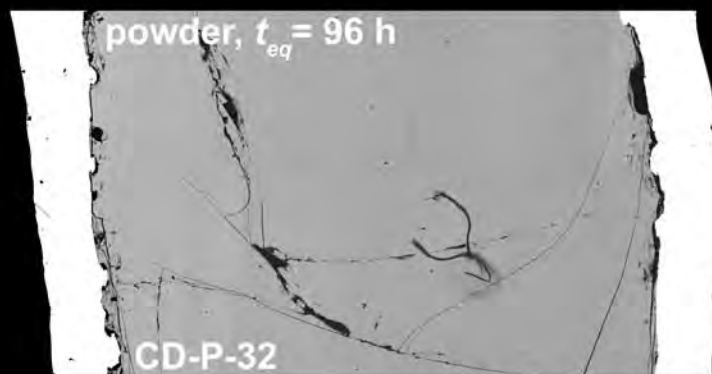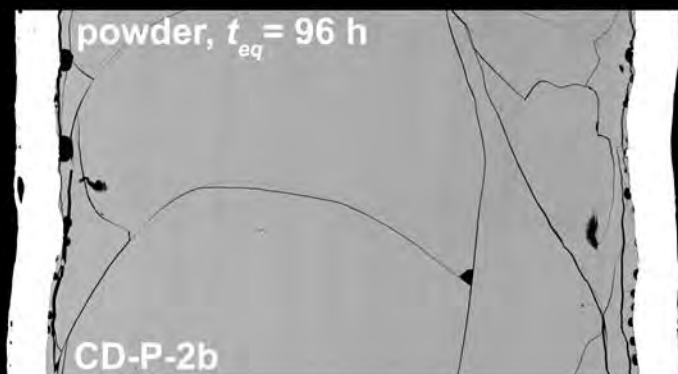
1mm

Figure 3

P_{final} = 100 MPa, 0.17 MPa·s⁻¹

cylinder, t_{eq} = 96 h CD-C-1

powder, t_{eq} = 24 h CD-P-1

CD-P-1

1mm

200 µm

Figure 4

(a) CD-C-2 eq: 96 h
CI cylinder

(b) CD-P-2b eq: 96 h
CI powder

(c) CD-C-25 eq: 96 h
VAD79 cylinder

(d) CD-P-32 eq: 96 h
VAD79 powder

10μm
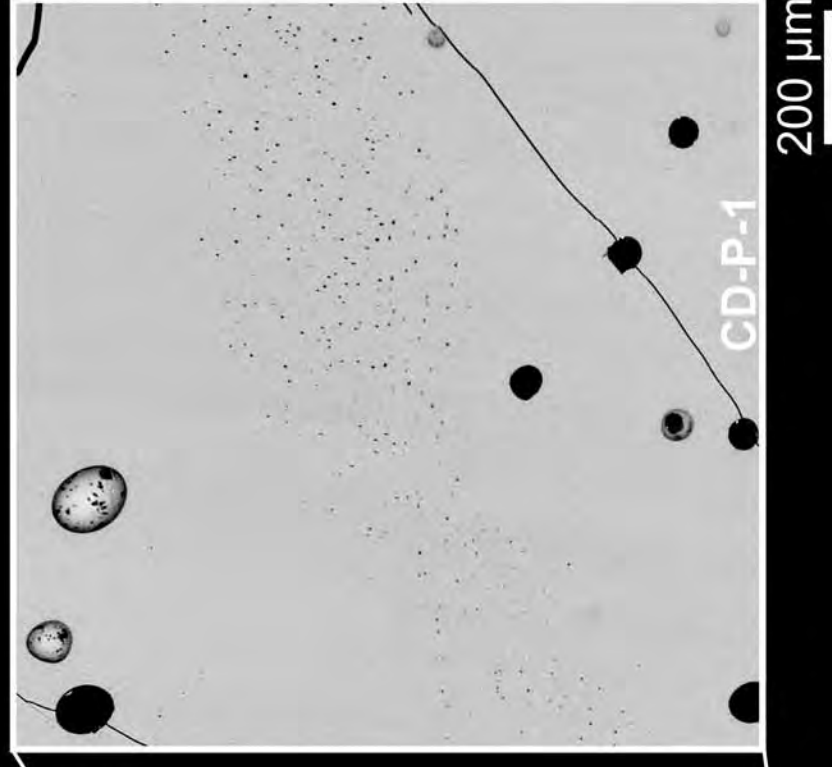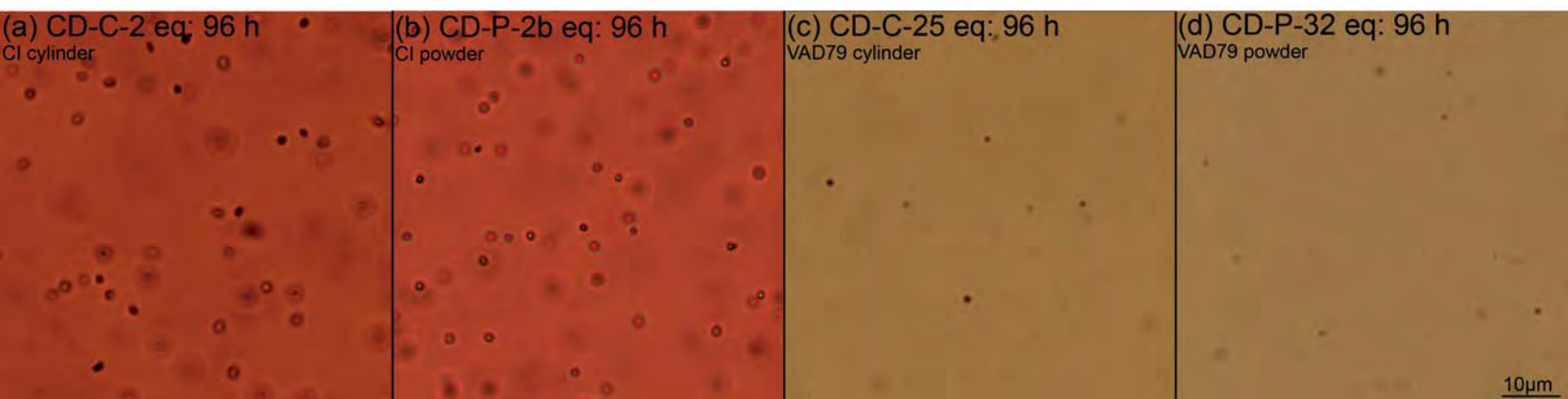
Figure 5

CD-C-1
P_{final} = 100 MPa
0.17 MPa·s^{-1}

5μm

crystal

10μm
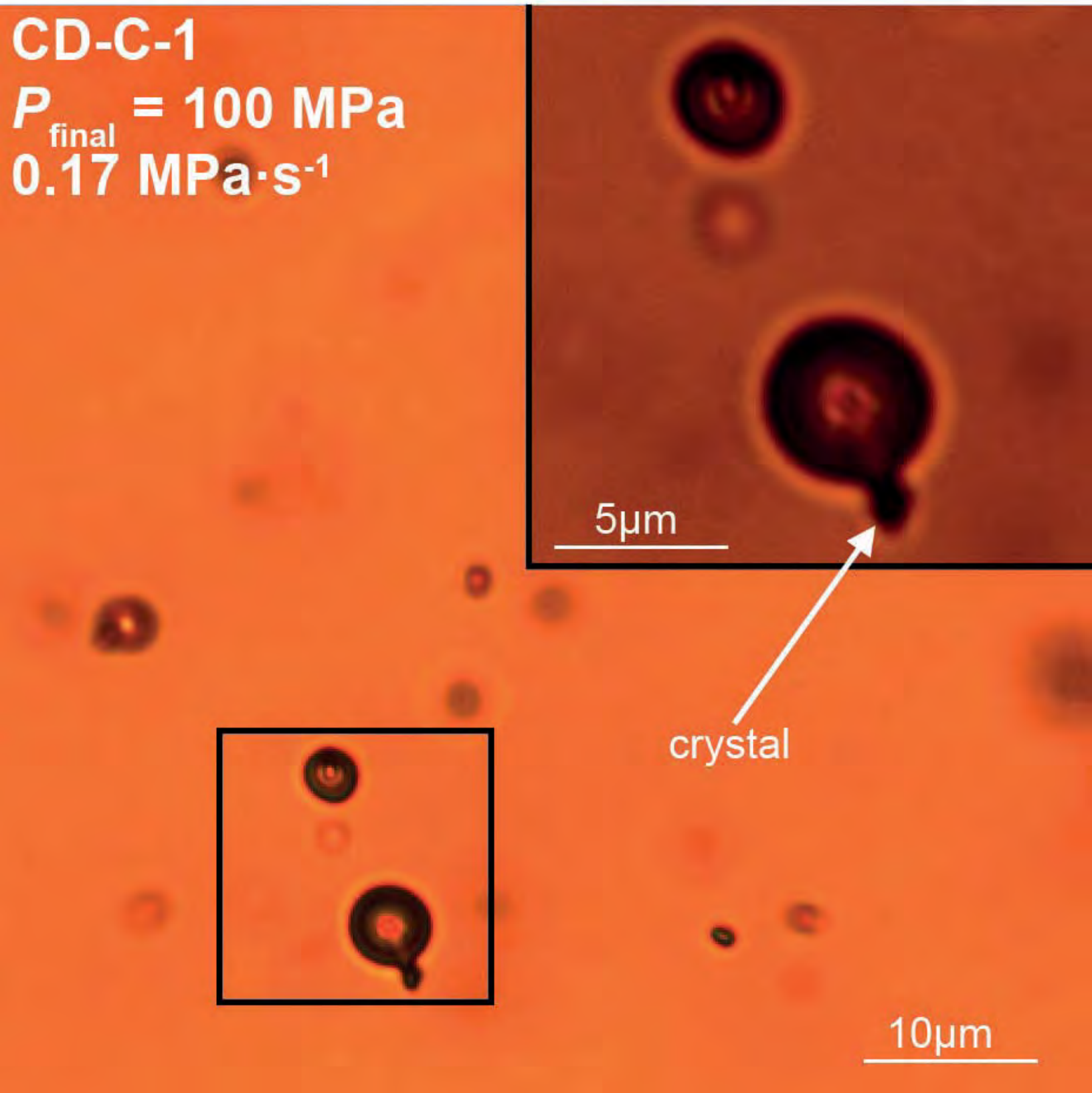
Figure 6

CD-C-3 - P_{final} = 75 MPa, 0.024 MPa·s⁻¹
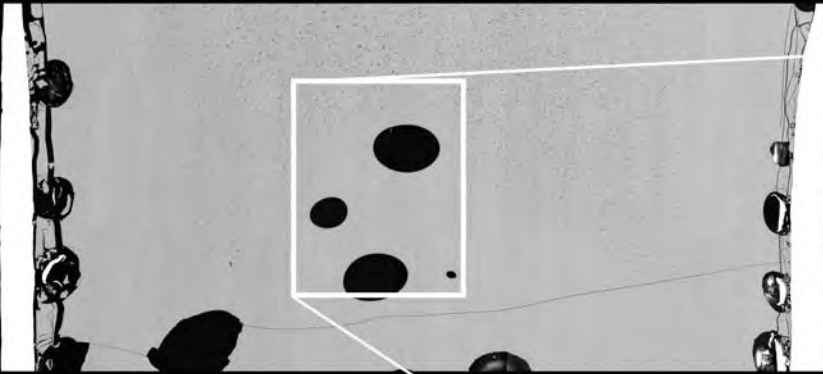
CD-C-4 - P_{final} = 75 MPa, 0.17 MPa·s⁻¹
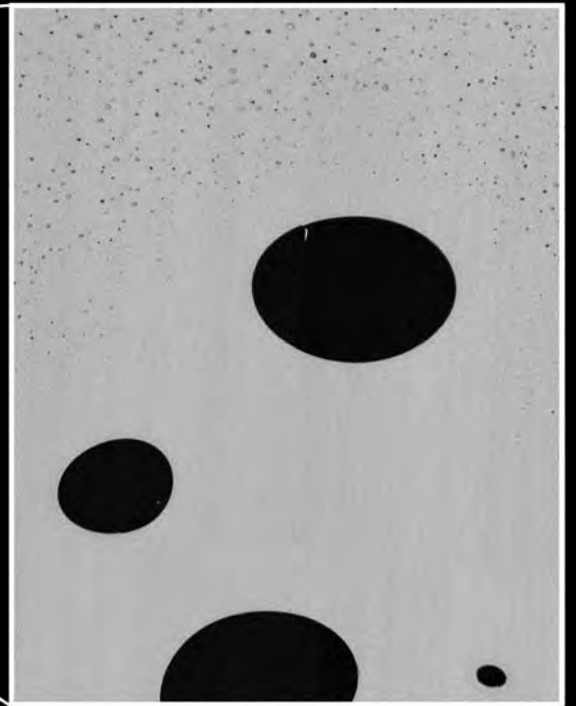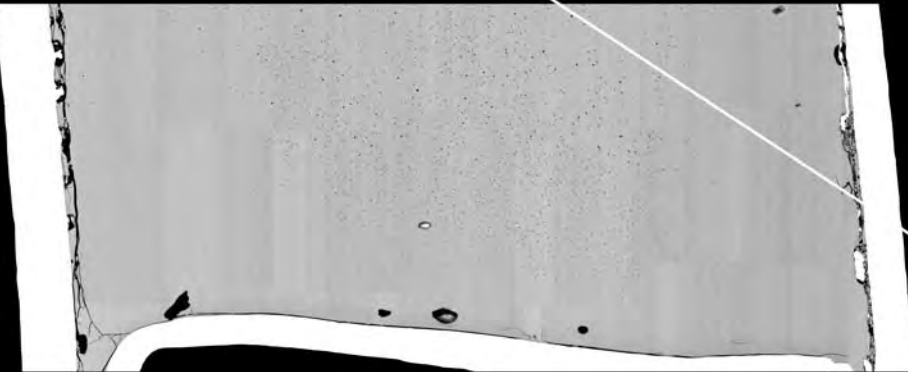
200 μm

1mm
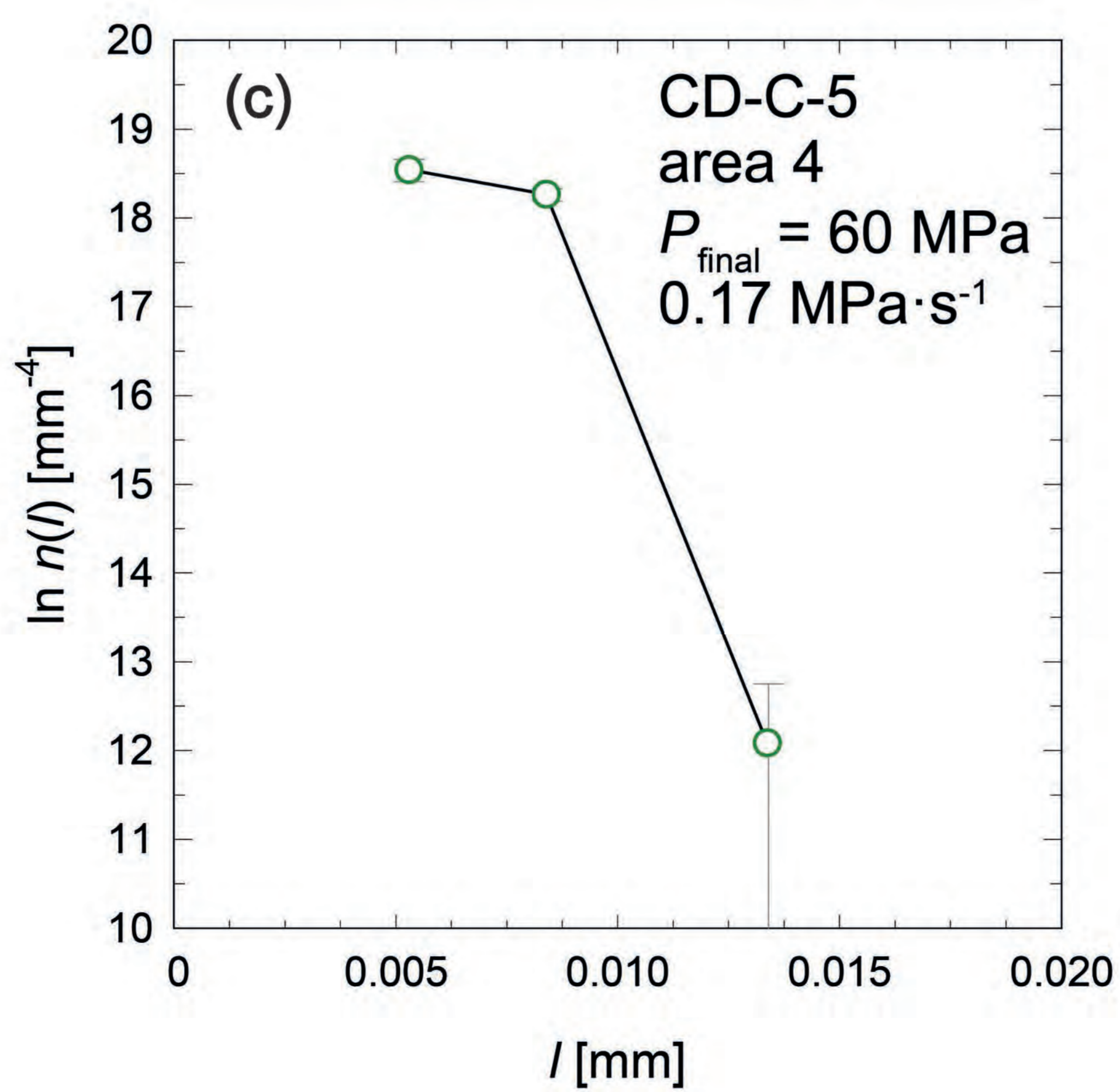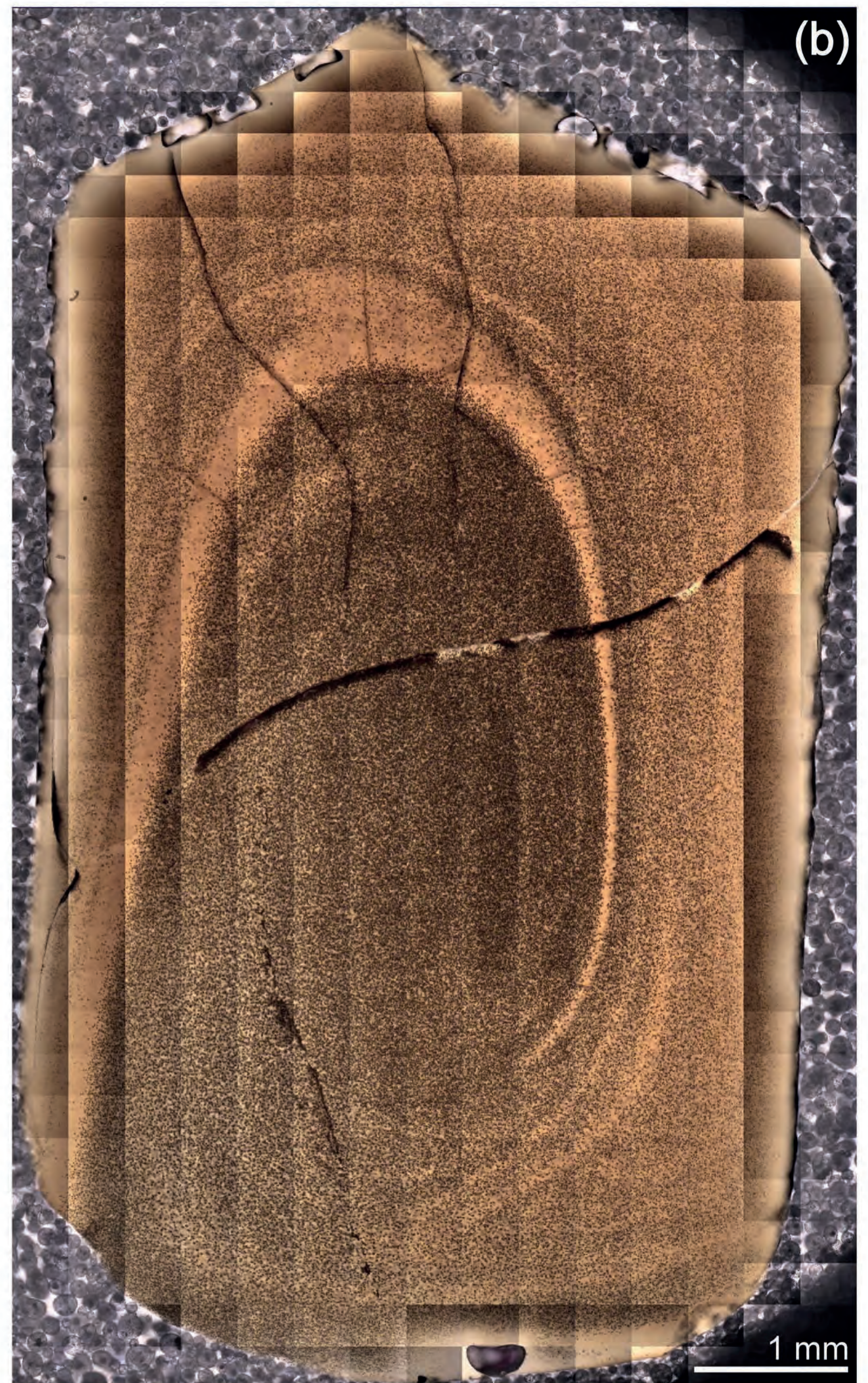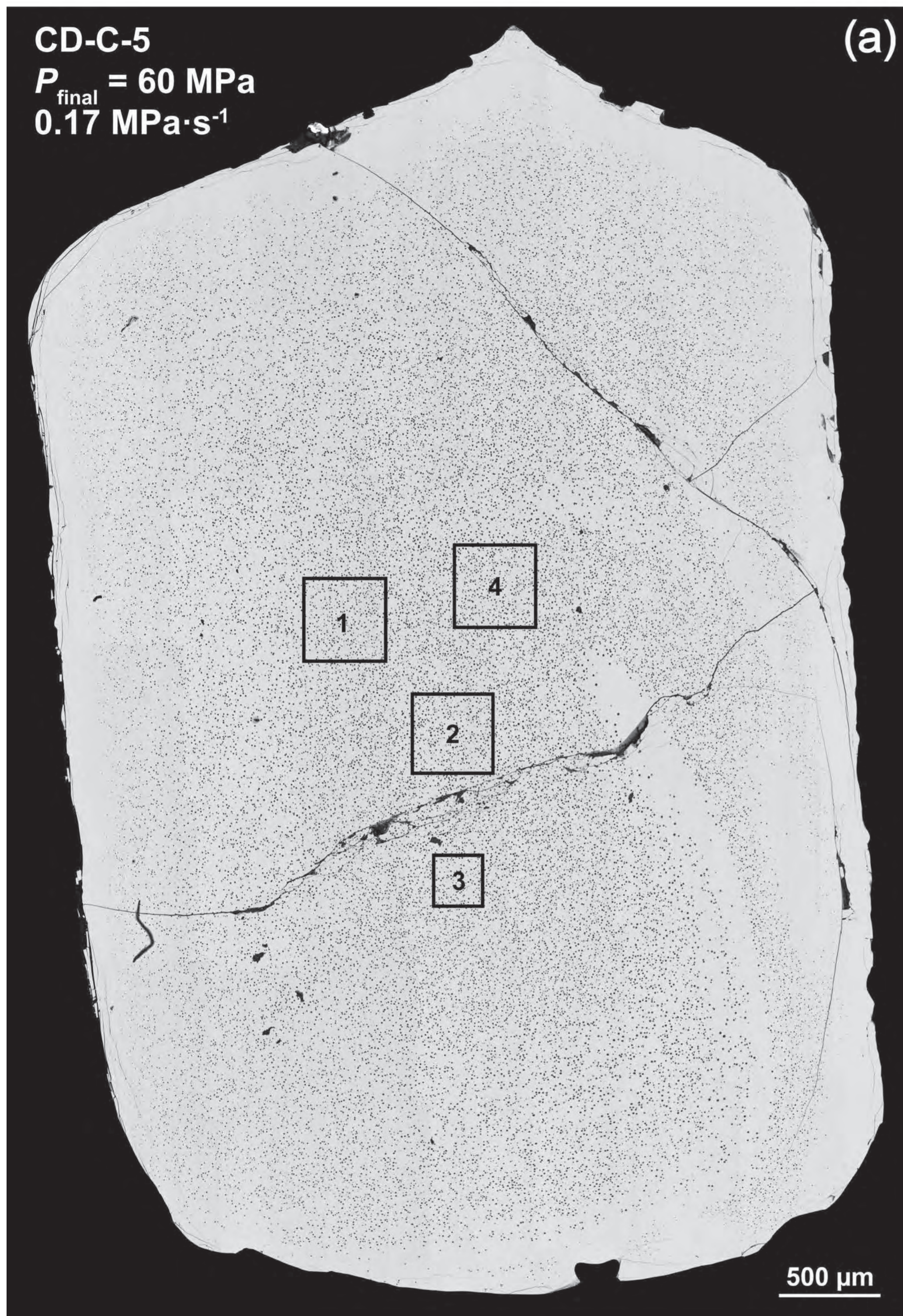
Figure 7

Figure 8
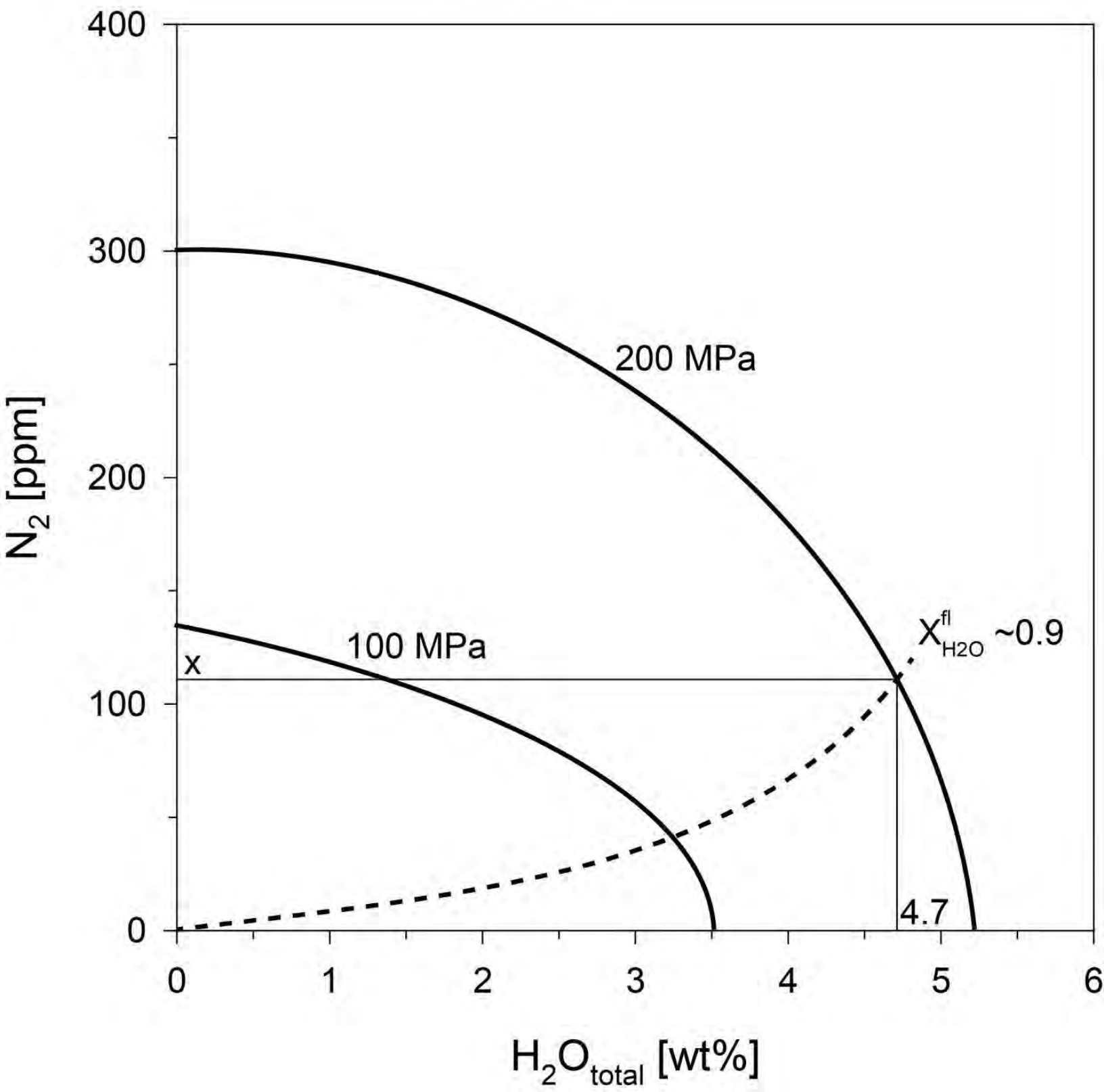
Figure 9
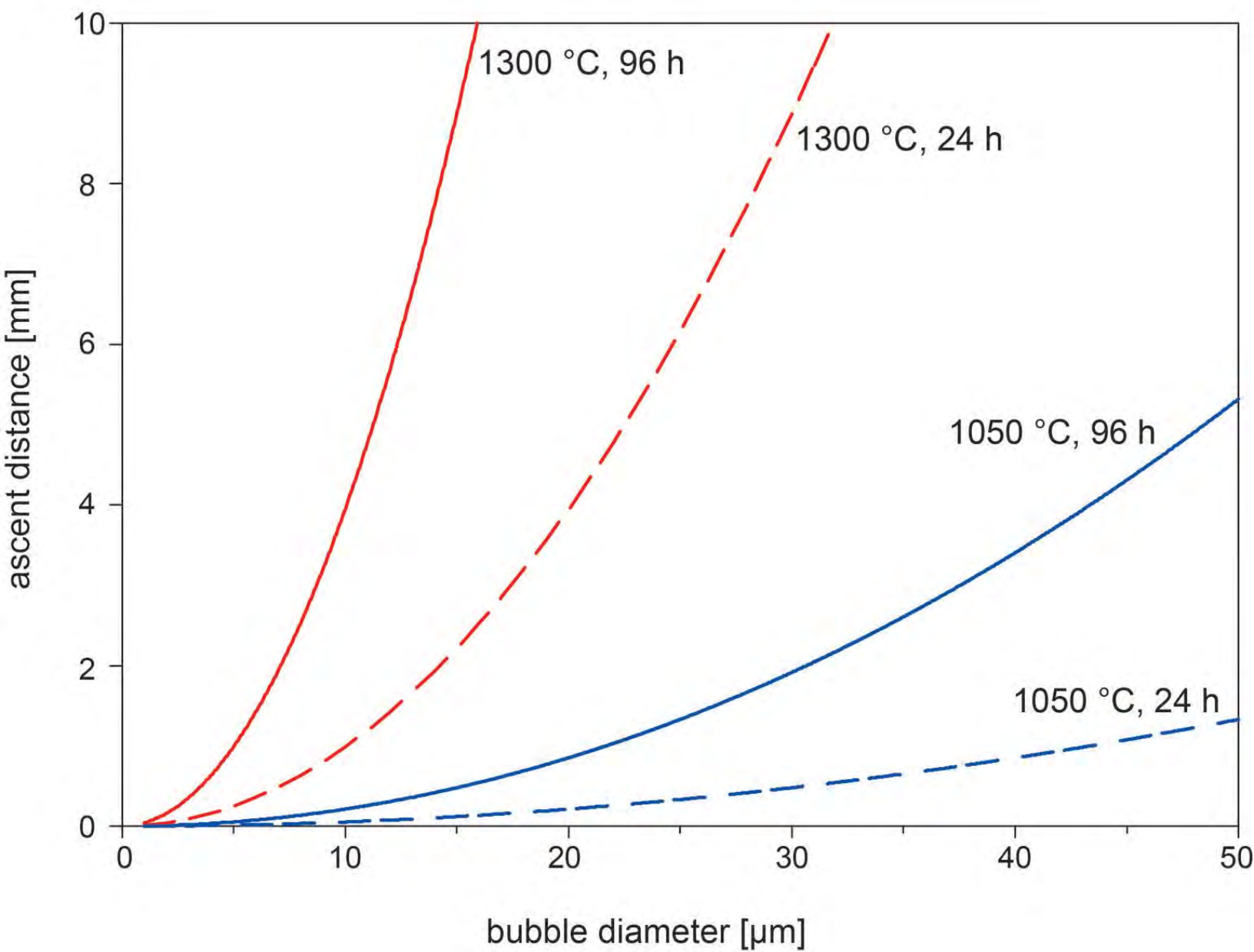
Figure 10

CD-C-4
P_{final} = 75 MPa
0.17 MPa·s^{-1}

10 µm

Figure 11

Legend:
- ▲ this study CI - cylinder
- ● this study VAD79 - cylinder
- ○ Ma15 - reduced $N_V(n)$
- ■ MS00 - not influenced
- □ MS00 - reduced $N_V(n)$
- ◆ ML02 - not influenced
- ◇ ML02 - reduced $N_V(n)$
- ⬡ Go11 - not influenced
- ⬡ Go11 - reduced $N_V(n)$
- - - - $\sigma = 0.042$ N·m^{-1}, $D(Si^{4+})$
- —— $\sigma = 0.133$ N·m^{-1}, $D(H_2O_t)$

y-axis: log $N_V(n)$ [mm^{-3}]

x-axis: dP/dt [MPa·s^{-1}]

coalescence